AIAA JOURNAL
Vol. 56, No. 2, February 2018

Turbofan Broadband Noise Prediction Using the Lattice Boltzmann Method

D. Casalino* and A. Hazir†
Exa GmbH, 70563 Stuttgart, Germany
and
A. Mann‡
Exa Corporation, Brisbane, California 94005

DOI: 10.2514/1.J055674

The present work describes a numerical reproduction of the 22-in source diagnostic test fan rig of the NASA Glenn Research Center. Numerical flow simulations are performed for three different rotor/stator configurations and one rotational speed, representative of an approach operating condition, by using the lattice-Boltzmann solver PowerFLOW. The full stage and nacelle geometries are considered, and results are compared to available measurements. Tripping the rotor blades results in a slightly more accurate noise prediction as a consequence of a more accurate prediction of the velocity fluctuations in the rotor wake over the whole blade span. Fourier circumferential analyses are performed for an intake and a bypass duct section with the intent of explaining the origin of some tonal noise components and comparing the present results to available literature results. Finally, the effects of adding an acoustic treatment in the intake is shown by directly resolving the unsteady flowfield in a single-degree-of-freedom honeycomb layer.

Nomenclature

C_{mx}	=	axial momentum coefficient
c_∞	=	freestream speed of sound
M_∞	=	freestream Mach number
R	=	microphone radial distance
u_x, u_r, u_θ	=	axial, radial, and tangential flow velocity components
θ	=	microphone angular location in the engine symmetry plane
ρ_∞	=	freestream density

I. Introduction

MODERN turbofan architectures with very high bypass ratios provide improved engine performances at lower primary jet exhaust velocities. Higher bypass ratios imply lower fan rotational speeds and lower primary jet exhaust velocities, but because of different velocity scaling laws, this typically results in higher fan-to-jet noise ratios in approach conditions. Lower fan tip speed, reduced number of fan blades compensated by increased blade chord, and optimal selection of the rotor/stator blade count typically result in higher broadband-to-tonal noise ratios. However, to limit the increase of the engine weight with the nacelle diameter, the axial extension of the nacelle must be reduced. This results in a reduction of the surface available for acoustic lining and in a reduction of the interstage distance. Because the liner is tuned at harmonics of the blade-passage frequency, and because a shorter interstage distance results in deeper and more coherent rotor wakes impinging on the stator vanes, the axial contraction of the engine should result in lower broadband-to-tonal noise ratios. From these arguments, it follows that, to perform fan versus jet noise and the fan tonal versus broadband noise tradeoffs, including the effects of liners, it is crucial to introduce noise prediction methods in the engine design cycles as early and as accurately as possible. Moreover, for underwing engine architectures, the jet versus fan noise tradeoff should take into account the engine installation effects due to the jet/flap interaction in approach/landing conditions.

State-of-the-art prediction methods used by industry, for jet and fan noise prediction, typically rely on semi-empirical or semi-analytical formulations, where the noise source statistics are derived from Reynolds-averaged Navier–Stokes (RANS) computations and transposed to far-field noise statistics through propagation models that take into account, at various degrees of approximation, the near-field diffraction and refraction effects. Such a methodology, which is based on a multitude of tools and methods, each one for one specific source mechanism, results in an additional layer of uncertainty due to the practical difficulty to manage the whole engine design space in a multidisciplinary framework. The use of high-fidelity numerical simulations able to tackle aerodynamic, aeroacoustic, and thermal design aspects in a homogeneous simulation environment (a single CAD model and computational fluid dynamics, or CFD, software), is the long-term solution for turbofan engine design. The goal of the present paper is to measure the fidelity of a hybrid lattice-Boltzmann (LB)/very large-eddy simulation (VLES) flow model [1–4] in predicting the absolute and relative broadband noise levels generated by a set of realistic fan/outlet guide vane (OGV) configurations and to demonstrate that accurate predictions can be already achieved in turnaround times that are compatible with industrial time constraints. It is worth mentioning that the usage of the LB/VLES solver PowerFLOW to accurately tackle unsteady flow problems of industrial relevance is an emerging practice. Thanks to the intrinsic low dissipation and dispersion properties of the LB scheme [5,6], the present solver has been successfully used in the field of aircraft aeroacoustics at both component [7,8] and full aircraft level [9,10]. A number of fundamental verification and validation studies have been also carried out in the past; Brès et al. [11] predicted the noise from a tandem cylinder configuration and proved a very good comparison with far-field noise measurements; Hao et al. [12] computed the acoustic diffraction from solid bodies and compared the numerical solutions to analytical solutions. Additionally, results of sound transmission through a constant-area duct are reported in this work with the intent of estimating the propagation error around the expected grid cut-off frequency.

Fan broadband noise predictions are currently performed through analytical formulations based on the combined use of gust/cascade aerodynamic response models [13–15] and infinite duct acoustic models [16–19], eventually taking into account some acoustic

Received 13 September 2016; revision received 29 July 2017; accepted for publication 8 August 2017; published online 22 September 2017.

*Senior Director, Department of Aerospace, Curiestrasse 4.
†Senior Application Engineer, Department of Aerospace, Curiestrasse 4.
‡Principal Engineer, Department of Acoustics, 150 North Hill Drive.

diffraction and swirl-flow refraction effects, such as the rotor shielding [20] and the acoustic mode trapping between rotor and intake [21], rotor and stator [22], and stator and exhaust [23]. The three-dimensional properties of the rotor wake are taken into account through specific axisymmetric empirical turbulence models and use of blade strip approach [19], or computed from radial profiles of statistical quantities extracted from RANS solutions [24]. The blade twist, sweep, and lean are taken into account by the cascade aerodynamic response model, but each blade section is approximated as a flat plate. An attempt to incorporate the aerodynamic response of a real airfoil in the fan noise model has been recently accomplished by Grace [25]. This analysis confirms the common opinion that the blade thickness and camber do not significantly affect the broadband noise levels, which result from a random wake/blade interaction process. Instead, modeling the real shape of the OGV blades is considered to be necessary for an accurate prediction of tonal noise because this depends on the interference between the waves generated by the periodic interaction between the rotor wakes and the stator vanes and thus on the accurate representation of the blade loading signature induced by the wake impingement. In spite of their elegance, there exists a certain conviction that these methods may not provide the correct trends for design variations around reference configurations without a specific validation and calibration. Moreover, the effect of nonaxisymmetric geometrical elements, like scarfed intakes and pylons in the bypass duct, cannot be taken into account without an additional layer of sophistication, and thus with additional uncertainties and computational costs.

The present analysis follows a previous one based on the same LB/VLES technology but different fan/OGV configuration. Mann et al. [26] used the Advance Noise Control Fan (ANCF) configuration of the NASA Glenn Research Center [27] to validate broadband and tonal noise prediction capabilities of PowerFLOW, with emphasis on the prediction of the modal duct content. Pérot et al. [28] used the same ANCF model to investigate the effect of a nacelle yaw angle on the radiated acoustic field and on the duct modal content. Casalino et al. [29] assessed the feasibility of a comprehensive fan/jet turbofan aeroacoustic simulation using a new LB formulation that covers the whole subsonic flow regime (M 0.95). The ANCF simulation was also repeated and provided very similar tonal and broadband noise levels. An overestimation of the overall noise levels up to about 5 and 3 dB in the forward and aft radiation arc, respectively, was reported. Very recently, a new PowerFLOW simulation campaign has been carried out for the ANCF configuration [30] to better investigate the effect of some uncertainties in the experiments and in the simulations. The main conclusions of all these studies are as follows.

1) The rotating microphone rake used in the ANCF experiment affects the duct modal content.

2) The CAD model used to build the computational mesh does not account for some details present in the test rig.

3) The presence of an inflow control device in the experiments and not in the simulations may have a nonnegligible effect on the ingested flow and on the forward far-field noise levels.

4) The absence of the tip gap in the simulation results in a more coherent rotor wake in the tip region, with a consequent overestimation of the periodic stator excitation.

It is a common opinion that the experimental data of the 22-in source diagnostic test (SDT) fan rig of the NASA Glenn Research Center [31,32], available in the framework of the AIAA Fan Broadband Noise Prediction Workshop, are affected by smaller uncertainties than the ANCF data. Furthermore, the SDT configuration is more suitable for the validation of broadband noise prediction tools. The present effort, therefore, has the main intent to better qualify the accuracy of a fan/OGV broadband noise prediction based on the last PowerFLOW release and version of the turbofan noise best practice simulation template.

In a previous work [29], the effect of an acoustic treatment in the intake was modeled by using an equivalent acoustic porous medium [33] tuned to a certain target frequency/impedance law. A bulk ceramic liner was used as a proof of concept, and results of tonal noise radiation from an axisymmetric intake were shown to be in agreement with frequency-domain finite element solutions of a wave equation for the acoustic potential in a nonuniform rotational base flow. As an alternative to liner modeling through an equivalent porous medium, which is not straightforwardly defined for a honeycomb liner due to the Helmholtz-resonance mechanism, Mann et al. [34] have evaluated the mesh resolution required to achieve reliable LB-VLES predictions of the absorption of a single-degree-of-freedom (1-DOF) honeycomb liner constituted of hundreds of cells and orifices. Following that pioneering work, a 1-DOF zero-splice honeycomb liner of realistic porosity and orifice diameter and specifically designed for the SDT tonal noise content is applied to the present SDT configuration, and results for an acoustically treated intake are also reported.

The paper is organized as follows. Information about the geometrical configurations and the computational setup are reported in Sec. II. In Sec. III, comparisons are shown between measured and predicted velocity fluctuations on an interstage plane section. Far-field noise results are presented in Sec. IV, together with the equivalent source power level. Results of an azimuthal Fourier analysis are reported in Sec. V. Finally, results for an acoustically treated intake and direct simulation of a 1-DOF honeycomb liner are reported in Sec. VI and compared to corresponding results for an untreated intake. The main findings of the present analyses are summarized in Sec. VII. Finally, a verification study is reported in the Appendix, which consists of computing the transmission of an acoustic mode through a constant-area annular duct.

II. Turbofan Configuration and Computational Setup

A. Turbofan Geometries

Figure 1 shows the nacelle of the SDT engine. The geometry is perfectly axisymmetric. To reproduce the stinger employed in the experiment, a cylindrical prolongation of the centerbody has been added to the CAD model provided by NASA. The rotor radius is 0.2786 m, the bypass exhaust radius is 0.2710 m, and the lip intake radius is 0.2962 m. The origin of the reference system used throughout is located in the midpoint of the rotor. The intake lip and bypass exhaust sections are located at $x = -0.3305$ m and $x = 0.5587$ m, respectively. Interstage hot-wire measurements have been performed by NASA in the plane $x = 0.1016$ m, referred to as station 1. The rotor is constituted of 22 blades, and the casing/blade-tip gap is about 0.5 mm. The location of the junction between the rotating spinner and the centerbody is at $x = 0.0424$ m. A detailed view of the 1-DOF honeycomb liner is also shown. For visualization purposes, portions of the perforated face sheet and honeycombs have been removed.

Figure 2 shows three variants of the OGV configurations: a 54-vane baseline radial OGV, a 26-vane low-noise swept OGV, and a 26-vane low-count radial OGV. All the other parts, with the exception of a small variations of the inner (less than 6.8 mm) and outer (less than 3.5 mm) casing profiles downstream of the OGV, are the same for the three configurations.

B. Operating Conditions

Among five values of the rotational speed tested by NASA, the one corresponding to the approach condition, say $\Omega = 817.652$ rad/s (7808 rpm), is considered in this work. This corresponds to a rotational tip Mach number of 0.6693 and a blade-passage frequency (BPF) of 2862.93 Hz. The ambient conditions are set to a temperature of 288.15 K and a pressure of 101,325 Pa. The engine operates at zero incidence in a freestream of Mach number 0.1. The Reynolds number based on average conditions at station 1 and the midspan rotor blade chord is 8.4×10^5. The freestream turbulence intensity is set to a value of 1%, but based on previous experience, this parameter is not expected to have a significant impact on the development of the unsteady flowfield in the fan stage.

C. Computational Setup and Mesh Resolution Effects

A sketch of the computational setup is shown in Fig. 3. The intake of the nacelle hosts a liner package that can be activated or deactivated. The rotor (red) and the spinner (orange) are

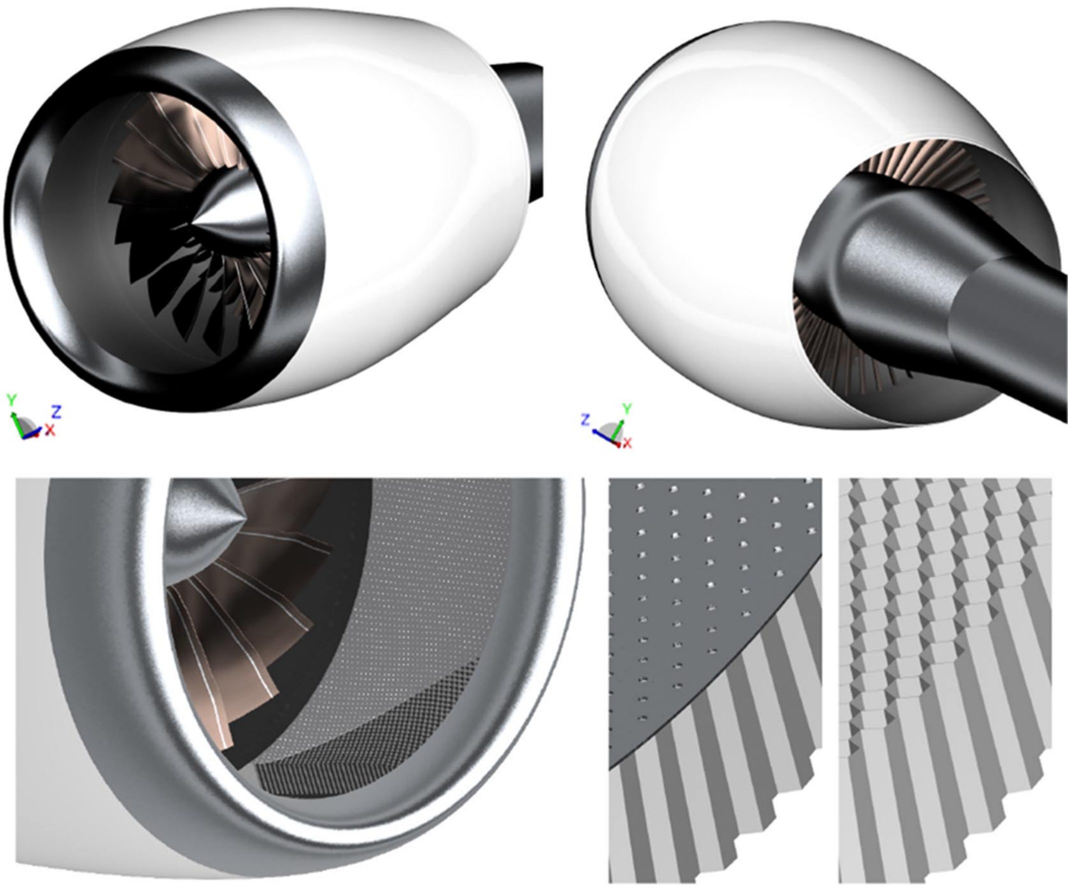

Fig. 1 Turbofan SDT baseline configuration: nacelle and details of the liner package.

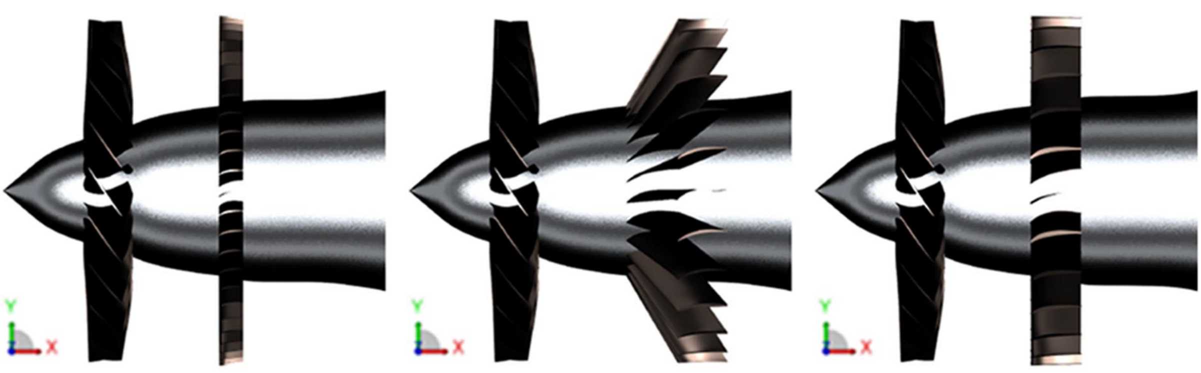

Fig. 2 Turbofan SDT configurations: baseline (left), low-noise (middle), and low-count (right).

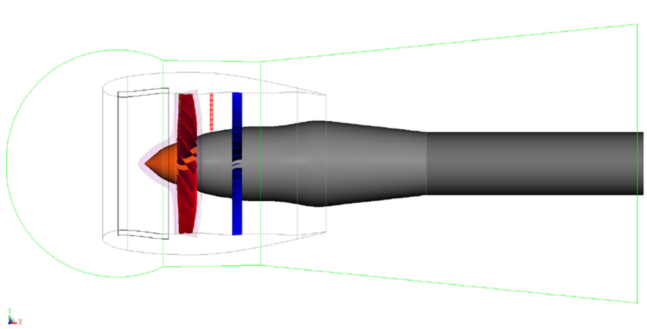

Fig. 3 Computational setup.

encompassed by a volume (purple) that defines the rotating mesh region. The centerbody (dark gray) is extended with a solid cylinder (light gray). As in the experiments, no primary jet is included in the simulation. The points (red) in the interstage denote the axial location of station 1. The Ffowcs Williams–Hawkings (FW-H) integration surface (green) used to compute the acoustic far-field consists of three parts: a spherical sector around the intake, a cylindrical connector, and a conical surface in the exhaust region. The cone is opened at its downstream extremity to avoid contamination of the acoustic signals due to integration of jet shear-layer hydrodynamic fluctuations. The downstream extension of the cone is, however, sufficient to recover the bypass duct radiation over the angular range of interest. The mesh on the FW-H integration surface is created automatically by the solver by intersecting the Cartesian lattice with the FW-H surface. The resulting mesh consists of about 4.5 million polygons, and its resolution is of the same order as that of the surrounding lattice, say 1.472 mm, about 15 grid points per acoustic wavelength at 15 kHz. Further details about the employed FW-H formulation and implementation can be found in [35,36].

Simulations have been performed by using slightly different computational setups and different values of the mesh resolution. PowerFLOW generates automatically a Cartesian volume grid

Table 1 Mesh resolution, number of mesh elements, and CPU time

Resolution	VRs	Δ, mm	Voxels	FEV (10^6)	FES (10^6)	CPU time (10^3), h
Extra coarse (no gap)	15	0.366	300	85	25	2
Coarse (no gap)	15	0.261	420	119	35	4
Medium-untripped	15	0.183	600	171	49	30
Medium$^+$-untripped	15	0.183	1223	405	49	65
Medium-tripped	16	0.122	429	69	27	16
Fine-tripped	16	0.092	916	136	36	60
Extra fine-tripped	16	0.070	1869	261	53	225

around a set of individual solid parts, starting from a value of the minimum hexahedral cell (voxel) size, a number of variable resolution (VR) levels, from the finest to the coarsest one, with changes of the voxel size between adjacent VRs by a factor of 2, and the definition of the VR regions. The real surface of the body is recovered automatically by intersecting the Cartesian mesh with the solid parts and generating a collection of polygons (surfel) [37,38]. Surfels are generated whenever a surface representation is necessary, for instance, in the definition of the boundary between a fixed volume mesh and a rotating volume mesh around a rotor. The boundary conditions are prescribed on the surfels and not on the nodes of the Cartesian mesh; therefore, high accuracy is preserved in the representation of complex shapes and complex rotating mesh boundaries. The four values of the mesh resolution used in the present study are reported in Table 1, together with the corresponding number of voxels, fine equivalent voxels (FEVs), and fine equivalent surfels (FESs). The fine equivalent elements represent the number of elements weighted by the time stepping rate, which is proportional to the mesh resolution level.[§] The overall CPU cost for 10 rotor revolutions is also reported. Notice that, for the fine-tripped case, which represents the current best CPU cost/accuracy tradeoff for a case with resolved blade tip gap, the overall CPU cost is about 60,000 h, corresponding to a turnaround time of about 3.5 days with 720 cores (Intel Xeon CPU E5-2680 2.80 GHz).

The extra coarse and coarse resolution runs have been executed in a preliminary stage of the activity with the intent of performing a setup sanity check and a mesh resolution study in terms of aerodynamic performances. For these two runs, the finest voxel size was not small enough to resolve the blade tip gap, which has been therefore removed by extending the blade radially and letting PowerFLOW manage the casing/blade overlapping. The axial momentum on the rotor, based on the rotor front surface, blade radius, and tip velocity, is plotted in Fig. 4a. The first extra coarse run has been executed for more than 45 rotor revolutions, but an adequate statistical convergence is reached after 10 rotor revolutions. The current best practice for this class of simulations is to perform a medium resolution run with gap over 10 rotor revolutions, and then use the last frame to seed a fine resolution run, which is executed with an initial settling time of few blade-passage periods. The overall CPU cost per geometry is therefore about 90,000 h. The medium$^+$-untripped setup has been derived from the medium-untripped one by doubling the mesh resolution in the interstage volume only. The fine mesh has been obtained by adding an additional VR region around the blade tip and around a trip on the rotor blade, as discussed hereafter. The reduction of the axial momentum by about 4% is due to a better resolution of the tip gap. The fine-tripped setup is then used as a reference for a mesh resolution study performed by applying global coarsening and refinement factors of 75% (medium) and 130% (extra fine), receptively. The effect of the global resolution variation is shown in terms of variation of the axial momentum coefficient in Fig. 4b. It confirms that a grid-independent solution is achieved for the aerodynamic loads.

The results reported later correspond to the medium untripped case (untripped), a medium$^+$ untripped case, obtained by doubling the mesh resolution in the interstage volume only (untripped fine), and a fine-tripped run (tripped). These three runs have the same VR mesh layout, with a voxel size of 0.366 mm past the rotor and stator blades. The effect of the global mesh refinement is also documented by comparing results obtained by running the rotor tripped cases with three different values of the global resolution.

Because of the very small leading- and trailing-edge radii, a finest VR region has been defined around the edges through cylindrical volumes of 1 mm radius, as shown in Fig. 5. The trips on the rotor blades are also shown in the same figure. These are obtained by offset of a chord segment of 1.5 mm in the normal direction by a distance of 0.37 mm (about four voxel cells per trip height) along the entire span.

D. Time-Averaged Flowfield

As a setup sanity check and adequacy of the mesh resolution in terms of aerodynamic performances, it is useful to compare the time-averaged flow solution to validated RANS results provided by NASA. Figure 6 shows the time-averaged velocity fields in the symmetry plane for the baseline configuration. Notice that the stage region is not available in the RANS results. Outside the stage region, LB/VLES and RANS results are in good qualitative agreement, with the main differences taking place in the secondary shear layer, where the PowerFLOW resolution is intentionally coarser than that required to resolve the turbulent mixing and thus the secondary jet noise, which is outside the present scope.

The predicted mass flow rate is compared to the measured ones for the three SDT configurations in Table 2. The discrepancy between measurements and simulations is around 1%, which is larger than the estimated experimental uncertainty based on the reported values by NASA [39] for the wind-tunnel total pressure (51 Pa) and inlet Mach number (0.0004). However, the achieved aerodynamic prediction accuracy should result in acoustic prediction uncertainties smaller than the noise measurement uncertainties of about 1 dB [39]. In other words, discrepancies between measured and predicted noise levels are unlikely to be due to a lack of accuracy in the prediction of the time-averaged flowfield.

III. Interstage Velocity Field

A. Phase-Locked Velocity Maps

Phase-locked average velocity maps at station 1 for the baseline configuration are shown in Fig. 7. Hot-wire measurements are compared to three sets of numerical results with the intent of investigating the effect of some setup modifications. The first set of results corresponds to untripped rotor blades. For reasons explained in the next paragraph, a second set of results was obtained by doubling the mesh resolution in the interstage region. Finally, a third set of results corresponds to a tripped rotor blade, the same resolution in the interstage region as for the first set of results, and a twice finer mesh resolution in the tip gap. The three set of numerical results do not exhibit significant differences and deviate from the measurements by less than about 10%. The axial component, in particular, is underestimated and exhibits a thicker boundary layer along the casing. The reason for this discrepancy, which is not consistent with the mass flow prediction accuracy, is not understood. An error is thus potentially affecting the stage total pressure, but this information is not currently available in the data set.

Corresponding rms velocity maps are also shown in Fig. 7. The three sets of numerical results exhibit clear differences in two regions: close to the casing and in the inner part of the rotor wake. A finer mesh resolution in the interstage results in significantly higher turbulent

[§]The solution in a twice coarser voxel is updated with a twice larger Δt and is therefore two times computationally cheaper.

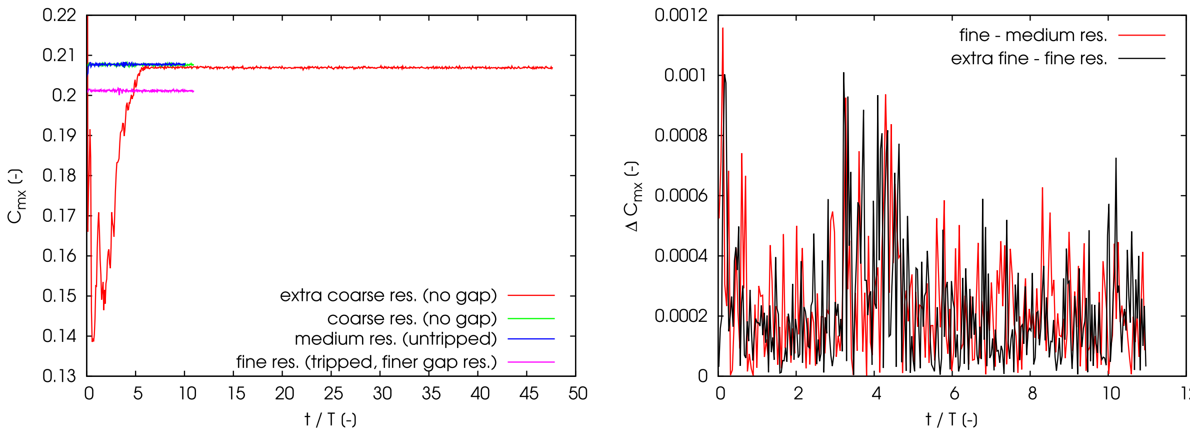

a) Influence of the computational setup **b) Influence of the global mesh resolution for the tripped cases**

Fig. 4 Rotor axial momentum coefficient for baseline SDT configuration and different computational setup and mesh resolutions.

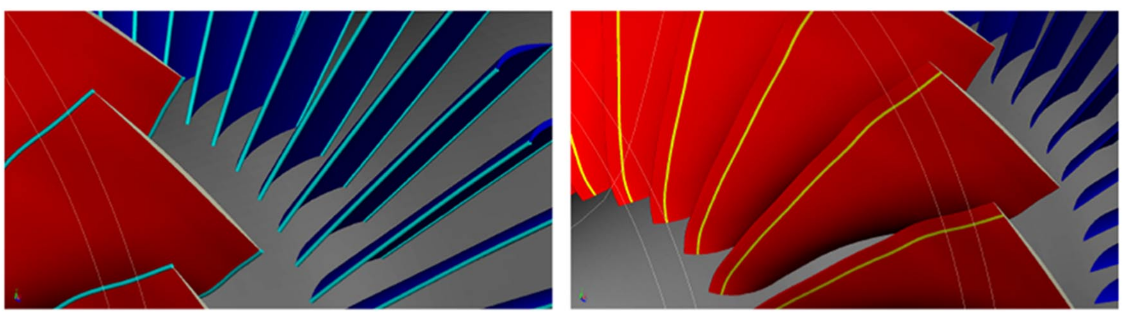

Fig. 5 Details of the computational setup: high mesh resolution regions around the blade edges (left), and trip on the rotor blade (right).

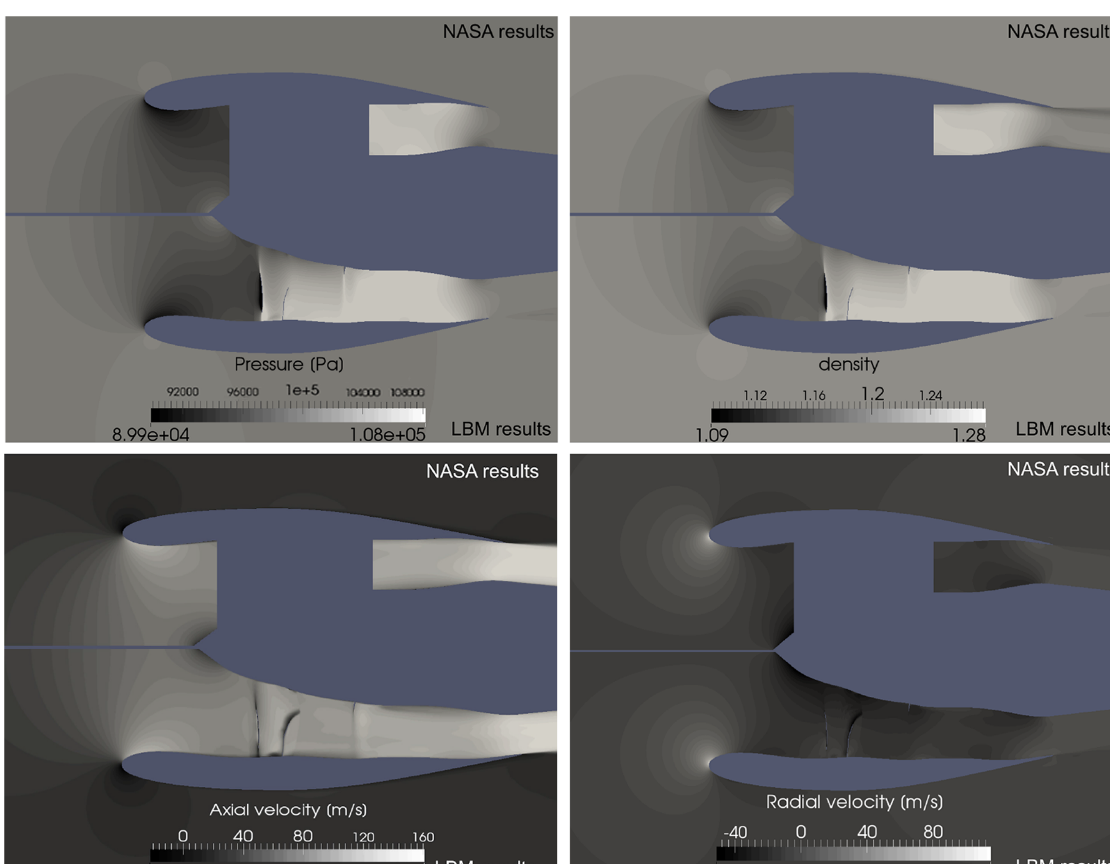

Fig. 6 Time-averaged flowfield on the symmetry plane. Comparison between NASA and PowerFLOW results. Pressure (top left), density (top right), axial velocity (bottom left), and azimuthal velocity (bottom right). SI units.

Table 2 Mass flow rate (in kilograms per seconds) for the SDT configurations

Configuration	Measurements	Simulations	Δ, %
Baseline (untripped)	26.54	26.25	1.09
Baseline (tripped)	26.54	26.18	1.36
Low-noise (tripped)	26.44	26.27	0.8
Low-count (tripped)	26.54	26.27	1.02

levels close to the casing and only slightly higher levels in the wake. Conversely, adding the trip produces only slightly higher turbulent levels close to the casing and significantly higher levels in the wake, in particular, closer to the blade root. Comparing these results to the hot-wire measurements reveals an overestimation of the turbulent levels close to the casing and in the outer radial part of the wake as well as a more accurate prediction of the turbulent levels in the root wake region. According to the authors' opinion, the presence of the trip in the simulation mitigates the effects due to a lack of rotor blade resolution to resolve an intrinsically intermittent low-Reynolds-number flow. The trip is perhaps not necessary for higher rotor speeds, but this needs to be verified with a new simulation campaign extended to different operating conditions.

A more quantitative comparison between measurements and simulations is shown in Fig. 8, where average and rms velocity components extracted along a vertical line at station 1 are plotted as a function of the blade span ratio. At this azimuthal location, the larger discrepancies between measurements and simulations have been observed in the contour maps of Fig. 7. Both the mesh resolution and the presence of the trip have a negligible effect on the average results. The mesh resolution has a weak influence on the rms quantities. This is also an indication of the fact that discretization errors at the interface between the stationary and rotating mesh regions should not have a significant effect. All the average results are in fairly good agreement with the measurements, but the radial component exhibits a systematic underestimation that needs a deeper investigation. The fluctuation levels in the rotor wake are dramatically underestimated by the untripped simulations. Conversely, the tripped results exhibit an underestimation of about 20% only, and this effect of the trip will be the object of future investigations. All the results exhibit a systematic overestimation of the fluctuation levels close to the casing. The origin of this issue is obscure at the present stage of the research. The influence of setup modifications will be investigated in the future to shed light on this issue.

B. Velocity Spectra

Narrow-band spectra of the velocity fluctuations at three radial locations are shown in Figs. 9–11. The length of the signals corresponds to 110 and 10 rotor revolutions for the hot-wire measurements and simulations, respectively. For both data sets, Fourier transforms are computed with a bandwidth of 28.6293 Hz, 50% window overlap, and Hanning weighting. Figure 9 shows results at one point very close to the casing. The three different PowerFLOW setups provide similar results, and both the mesh resolution in the interstage region and the blade trips have a small but consistent effect, in particular, at frequencies higher than 4–5 BPF harmonic counts.

Spectra at 80% radial location are plotted in Fig. 10. Broadband results for the tripped case are in better agreement with the measurements than for the other cases. Finally, spectra at 60% radial location are plotted in Fig. 11. At this location, only the broadband levels of the tripped case are in good agreement with the measurements but only below a harmonic count of about 3–4. Beyond this frequency, the velocity fluctuations are underestimated by almost one order of magnitude. The azimuthal velocity fluctuation for the tripped case is underestimated by about one order of magnitude beyond a harmonic count of 1. Fluctuations levels for the untripped and untripped-fine cases are underestimated by two/three orders of magnitude. These results are of course consistent with the rms velocity maps shown in Fig. 7. It is worth mentioning that, compared to the results reported in [40], the present radial and

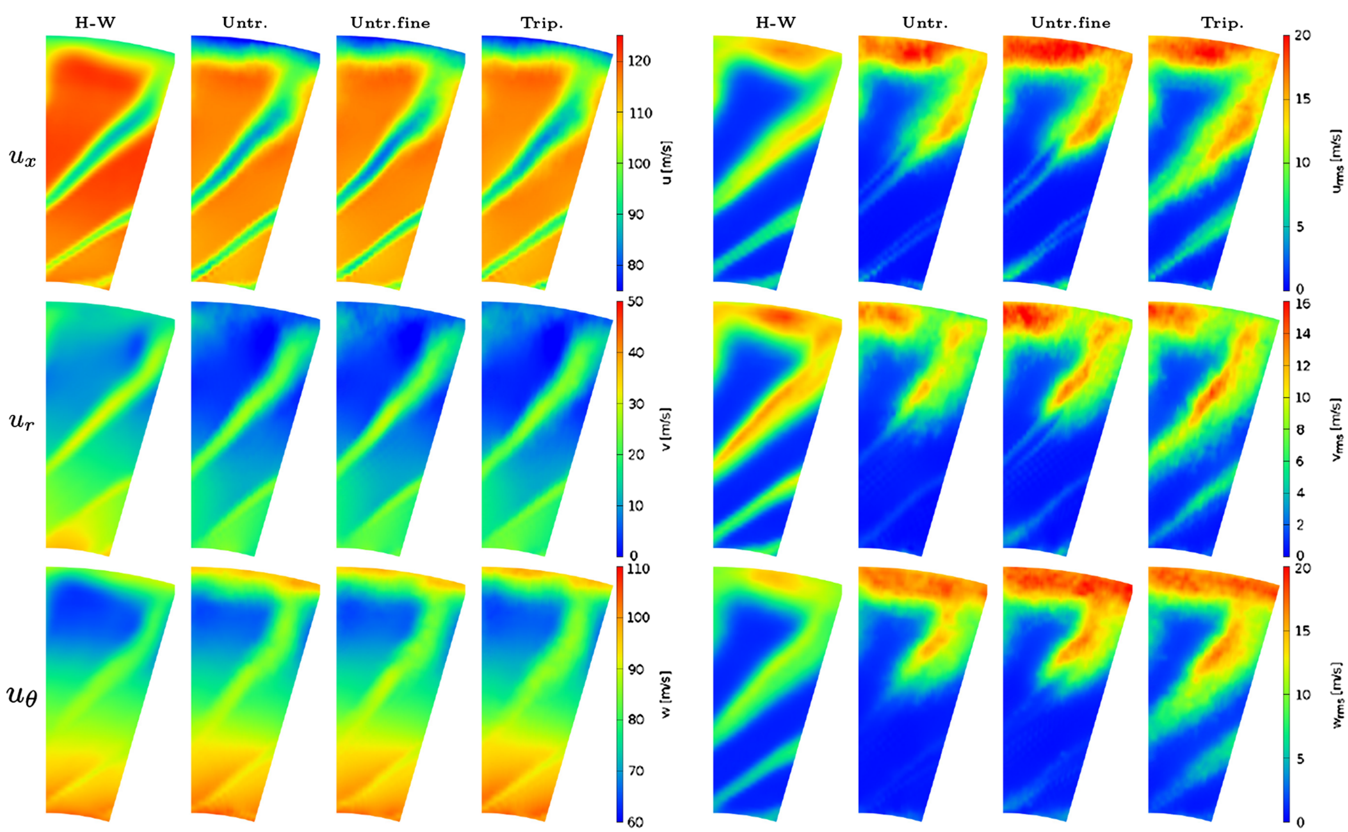

Fig. 7 Phase-locked average (left block) and rms velocity (right block) at station 1. Axial, radial, and azimuthal velocity in the top, middle, and bottom rows. Hot-wire measurements on the left column, PowerFLOW results for untripped, untripped-fine, and tripped cases from second to forth columns.

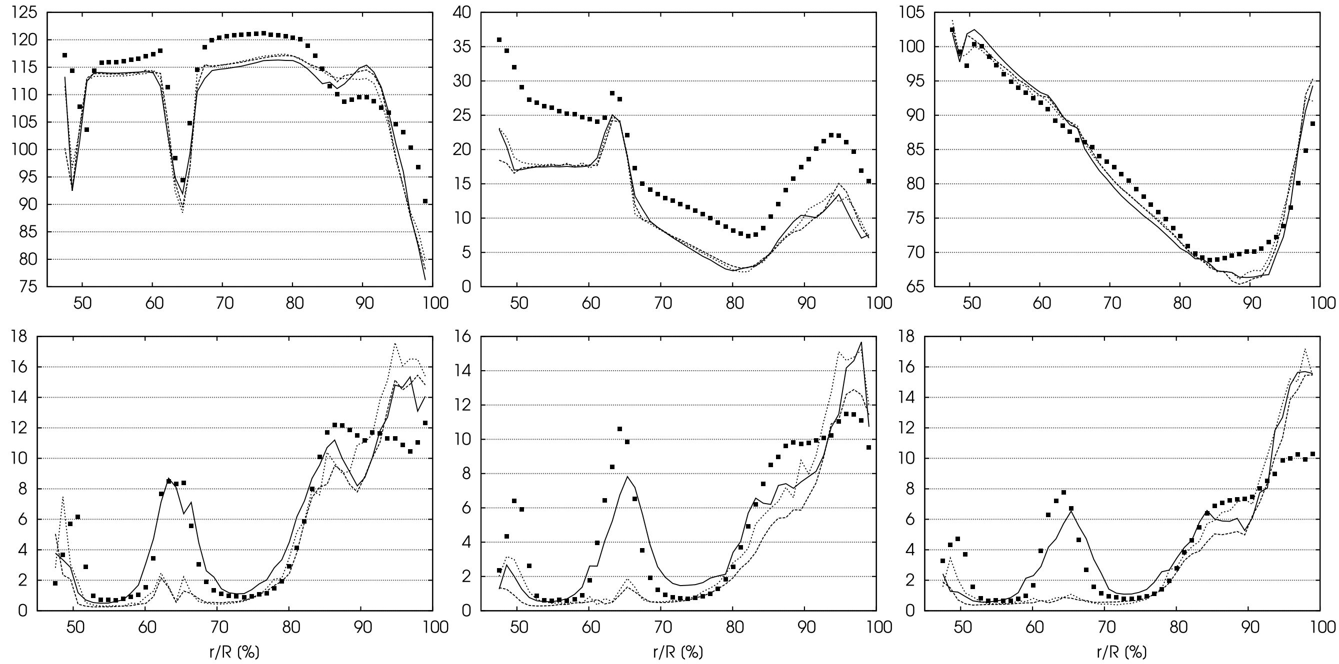

Fig. 8 Line cuts of the phase-locked average (top) and rms velocity (bottom) (in meters per second). Axial, radial, and azimuthal velocity in the left, middle, and right columns, hot-wire measurements (symbols) and PowerFLOW results for untripped (dotted lines), untripped-fine (dashed lines), and tripped (lines) simulations.

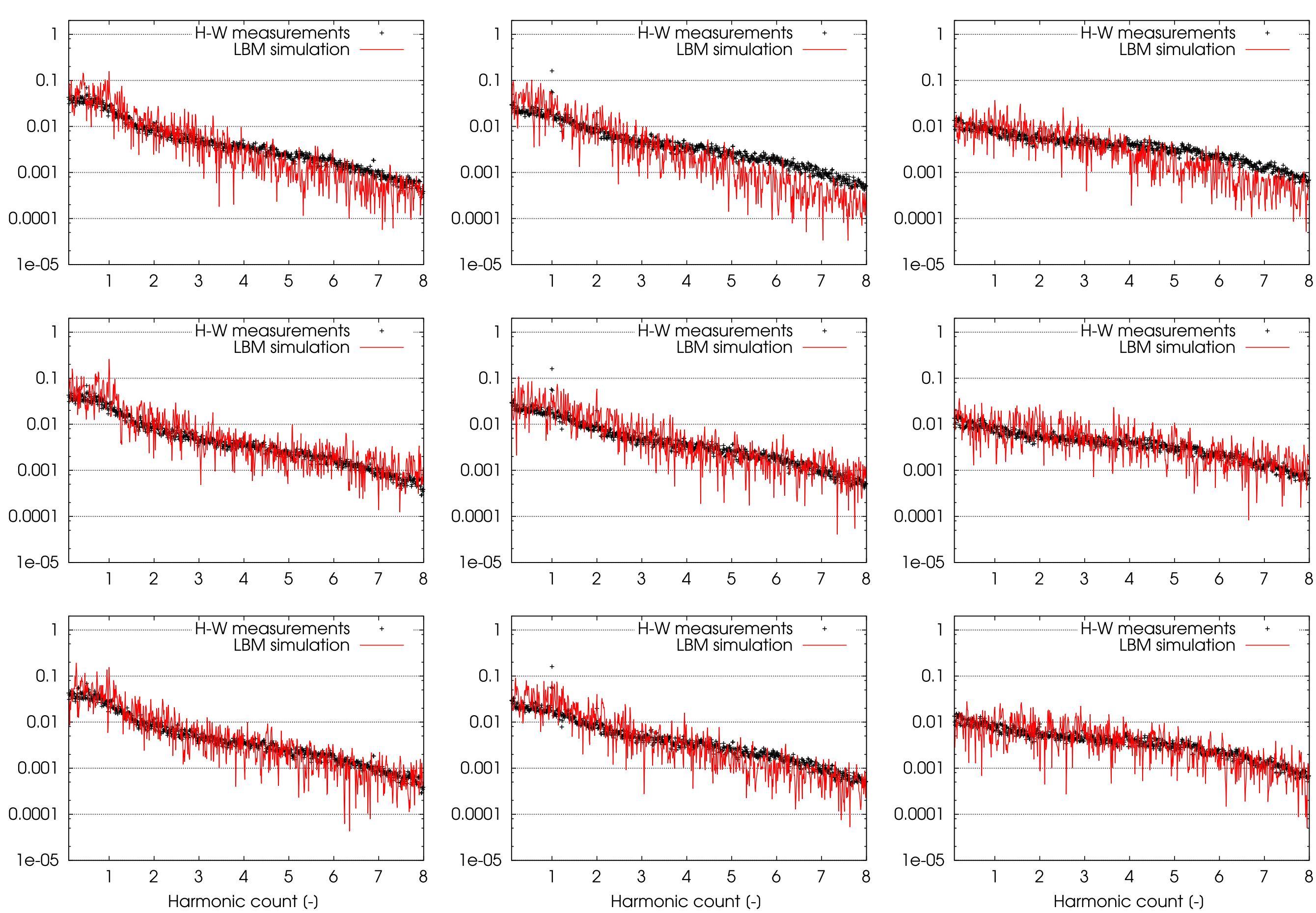

Fig. 9 Velocity spectra at $r = 0.275997$ m. Axial, radial, and azimuthal velocity in the left, middle, and right columns, (in meters per second) hot-wire measurements (symbols) and PowerFLOW results for untripped (top), untripped-fine (middle), and tripped (bottom) cases.

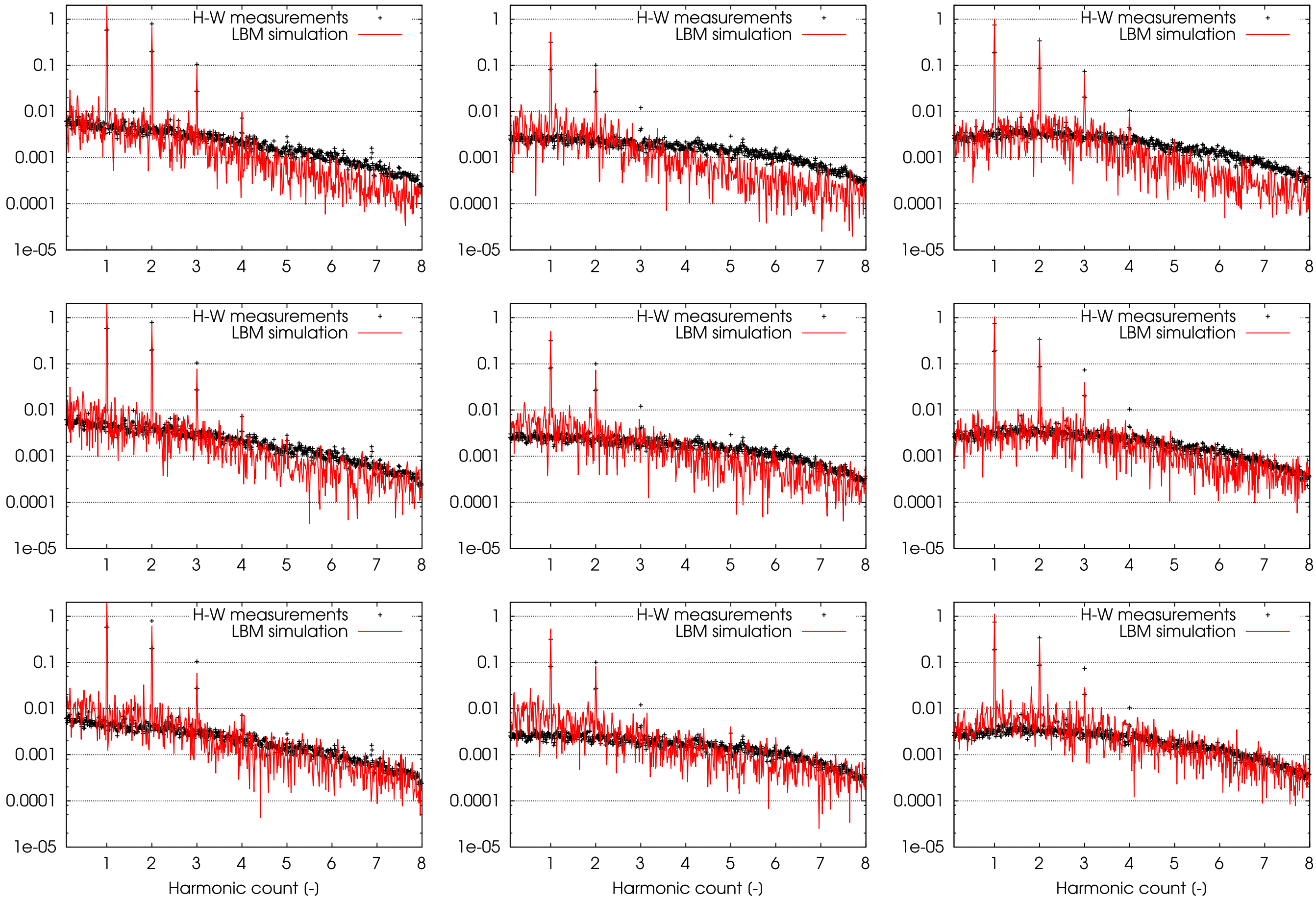

Fig. 10 Velocity spectra at $r = 0.223292$ m. Axial, radial, and azimuthal velocity in the left, middle, and right columns, (in meters per second) hot-wire measurements (symbols) and PowerFLOW results for untripped (top), untripped-fine (middle), and tripped (bottom) cases.

azimuthal velocity spectra, and in particular the tonal components, are in better agreement with the measurements. This is due to a previous postprocessing mistake, resulting in switched radial and azimuthal velocity components.

The effect of global mesh refinement for the tripped cases is finally shown by plotting in Fig. 12 the absolute value of changes in the velocity spectra referred to the tip velocity. A consistent behavior is observed, in particular for the tonal components.

IV. Far-Field Noise and Source Power Level

Far-field noise results obtained by integration of the FW-H equation on the permeable surface plotted in Fig. 3 are presented in this section. Three sets of results are reported.

1) Narrow-band noise power spectral density (PSD) spectra in decibels per hertz at several angular locations on a circular array of 10 m radius, with a constant angular spacing of 5 deg, from 30 deg (front) to 150 deg (aft).

2) Overall sound pressure level (OASPL) in decibels on a linear sideline array 2.25044 m away from the engine axis, with a constant angular spacing of 5 deg of the microphones, from 30 to 140 deg. To avoid jet noise and rig noise contributions in the measurements, the OASPL is computed from 1.2 to 50 kHz.

3) One-side narrow-band source power level (PWL) in decibels per hertz, computed by integration of the acoustic intensity over the spherical surface portion corresponding to the aforementioned circular array, using the following formula:

$$\mathrm{PWL}(f) = \int_{\theta_{\min}}^{\theta_{\max}} 2\pi R^2 \sin(\theta) \frac{[1 + M_\infty \cos(\theta)]^2 \mathrm{PSD}(f, \theta)}{2\rho_\infty c_\infty} \, \mathrm{d}\theta \quad (1)$$

where R is the array radius; θ is the radiation angle varying from $\theta_{\min} = 30$ deg to $\theta_{\max} = 150$ deg (clockwise); M_∞ is the freestream Mach number; and ρ_∞ and c_∞ are the ambient density and speed of sound. The PSD is expressed in square pascals per hertz, and the value of PWL is then converted to decibels. The integration is performed using a Simpson formula. This expression of the power level does not account for the difference between emission and geometric angles that can be neglected at the present value of M_∞.

All the results have been obtained by performing an azimuthal average of the signals computed at four azimuthal angles (every 90 deg). More precisely, signals cropped at an integer number of blade-passage periods have been appended. Therefore, for every microphone location on both the linear and circular array, a signal duration of almost 40 rotor revolutions has been used. The Fourier transforms have been performed with a bandwidth of 28.6293 Hz and Hanning weighting.

Figure 13 shows the effect of the computational setup for the baseline configuration on the noise spectra at two angular locations corresponding to the angles of maximum front and aft radiation. The effect of increasing the interstage mesh resolution and tripping the blade is higher at the aft microphone, and this is consistent with the fact that the main effect is to increase the wake/OGV interaction noise, which is prominently transmitted through the bypass duct. The overall setup effect on the aft radiated noise is a uniform shift of about 4 dB over the whole frequency range.

The OASPL levels along the linear array and the PWL spectrum are shown in Fig. 14. Tripping the blades allows to recover the right ratio between maximum front and aft radiation, thus resulting in a more consistent discrepancy with the measurements of about 1 dB in the forward and aft radiation lobes. The far-field noise measurement uncertainty is estimated to be in the order of 1 dB [39]. The mesh

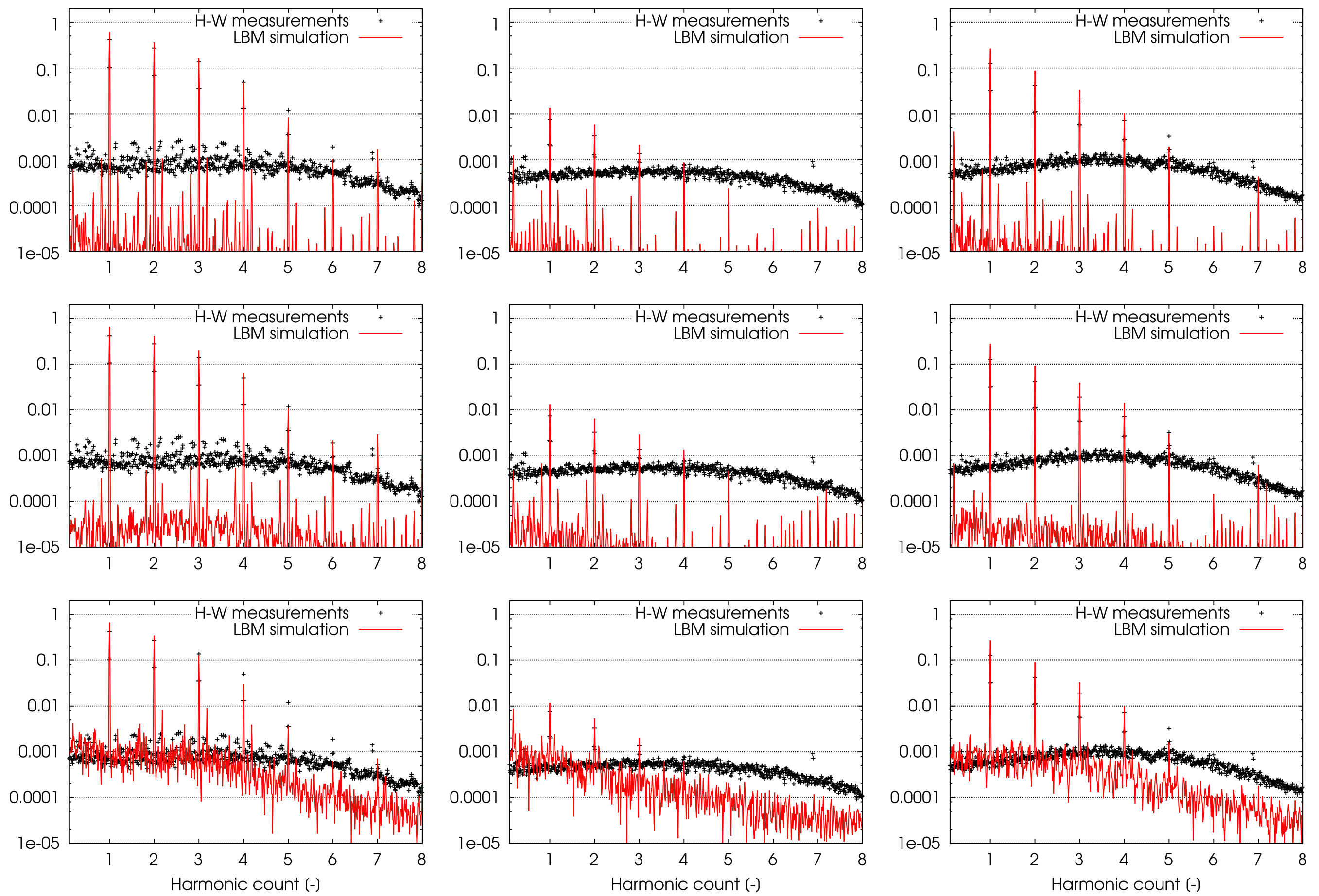

Fig. 11 Velocity spectra at $r = 0.167640$ m. Axial, radial, and azimuthal velocity in the left, middle, and right columns, (in meters per second) hot-wire measurements (symbols) and PowerFLOW results for untripped (top), untripped-fine (middle), and tripped (bottom) cases.

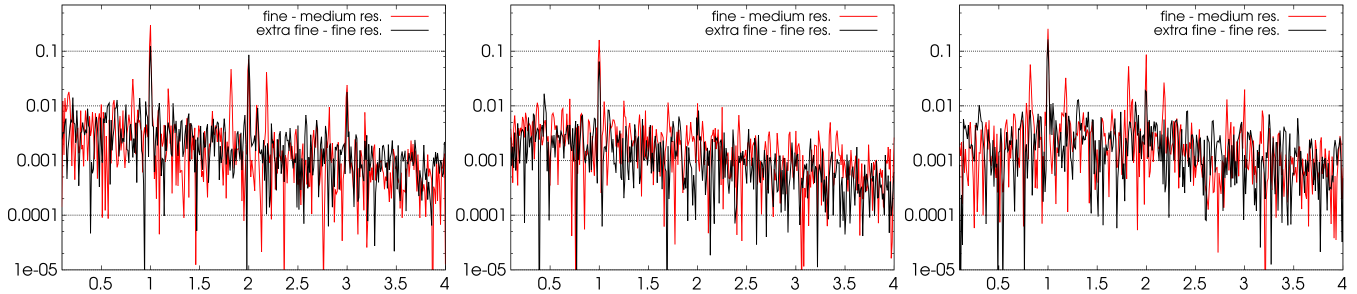

Fig. 12 Velocity spectra at $r = 0.223292$ m. Axial, radial, and azimuthal velocity in the left, middle, and right columns, plotted as percentage of tip velocity difference between results for three values of the mesh resolution.

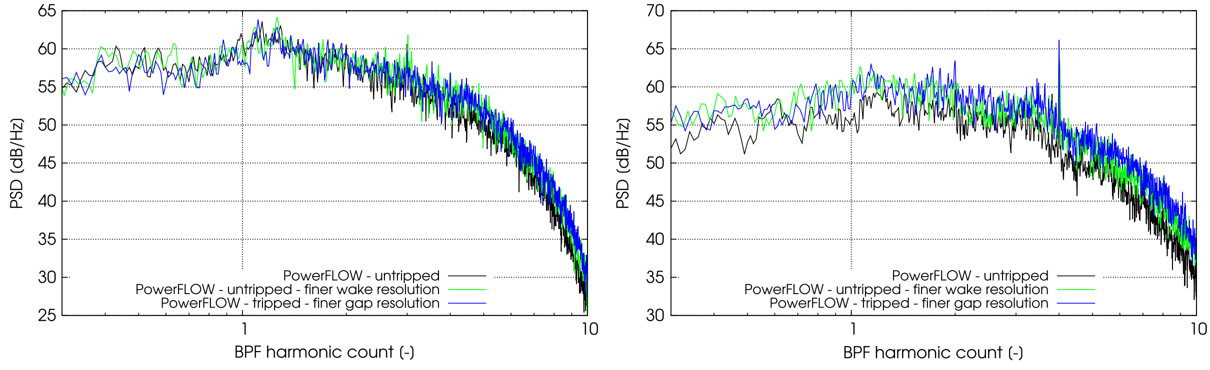

Fig. 13 Effect of computational setup on the far-field noise spectra at a distance of 10 m and angular location of 50 deg (left) and 125 deg (right).

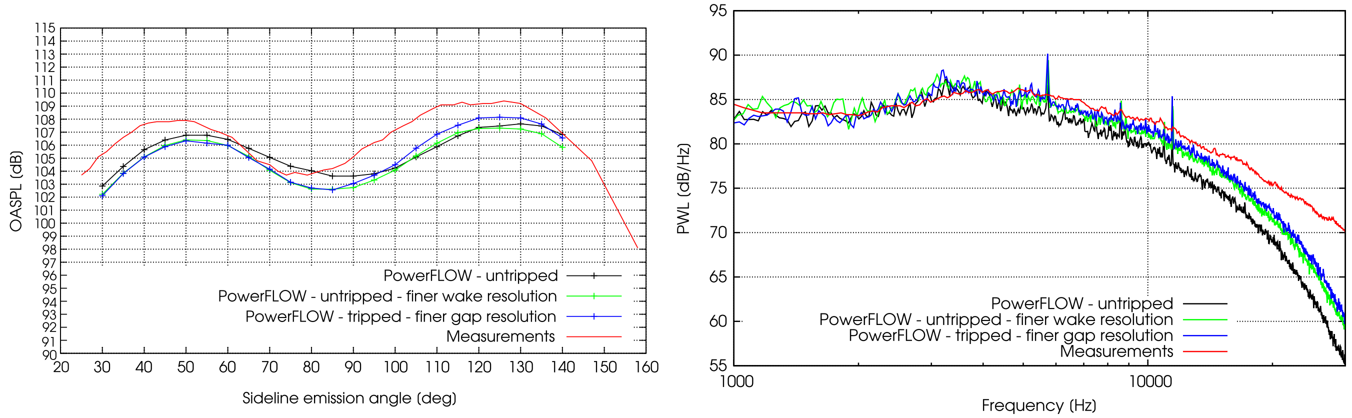

Fig. 14 Effect of computational setup on far-field OASPL along the sideline array (left) and PWL (right).

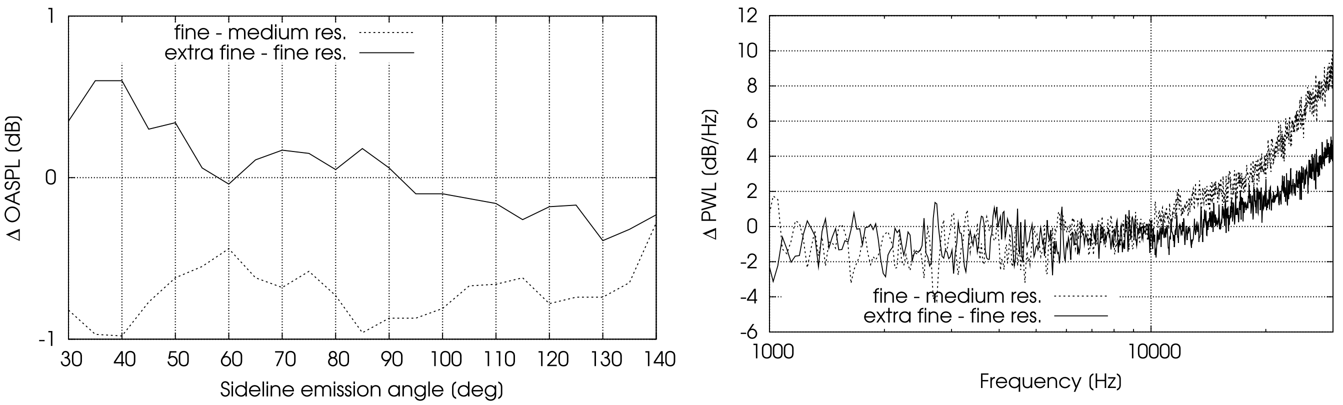

Fig. 15 Effect of global mesh resolution on far-field OASPL along the sideline array (left) and PWL (right).

cut-off frequency for the present simulation is expected to be about 15 kHz (~5 BPF). Beyond this frequency, the progressive deviation of the prediction from the measurements is not only due to a lack of fine resolved turbulence scales but also to the dissipation of the acoustic waves in the propagation from the fan/OGV to the FW-H surface. The 1 dB OASPL underestimation is likely due to the progressive loss of accuracy beyond the cut-off frequency.[¶] Consistent with the far-field OASPL levels, the tripped simulation provides higher PWL values than the two untripped simulations.

The effect of a global mesh refinement for the tripped simulations is shown in Fig. 15 by plotting incremental changes in OASPL and PWL. Both quantities exhibit a consistent grid convergence trend. More specifically, the PWL results are almost grid-independent up to 10 kHz.

The effect of the different OGV configurations is now illustrated by comparing three sets of tripped blade results. Figure 16 shows the OGV effect on the noise spectra at 30 and 125 deg. Both angular locations reveal that the low-noise and low-count OGVs generate lower broadband noise levels. However, the tonal content is very different. At the front microphone, for instance, the low-count OGV produces clear tones at 1BPF, 2BPF, and 4BPF. For the other OGVs, the broadband levels overwhelm the tones, with the exception of 3BPF for the baseline OGV. For all OGVs, some subharmonic components of 1BPF can be observed, which are likely to be due to the interaction between the rotor tip vortices and the blades. Because of the viscous effect of the wall, the tip gap vortices rotate at a lower speed than the blades. As a consequence, interactions with the rotor blades take place at a statistically smaller frequency than the rotational frequency.[**] The noise spectra at the aft microphone exhibit a clear noise reduction trend of the low-noise and low-count OGVs, starting from about 3 kHz. However, as for the front microphone, the tonal content is very different for the three configurations. A strong 1BPF tone takes place for the low-noise and low-count OGVs, which emerges by 10 and 15 dB for the two configurations, respectively. The 2BPF tone is very strong only for the low-count OGV; the 4BPF tone takes place only for the baseline OGV and the 5BPF only for the low-count OGV. The different tonal content is of course due to a different duct modal content in the engine, as discussed in Sec. V.

The OASPL levels along the linear array and the PWL spectrum for the three fan stages are shown in Fig. 17. All the effects observed in the far-field spectra can be observed also in these results, in particular, a clear broadband noise reduction trend associated with the lower OGV count and a different tonal noise content. Interestingly, both low-count designs are louder than the baseline OGV at radiation angles larger than 130–140 deg. This can be explained with the occurrence of duct modes in the bypass duct with a dominant shallow radiation attitude. The overall sound levels are underestimated by about 1.5 and 1 dB in the front and aft, respectively. The measurement uncertainty for this quantity is ± 1 dB.

Finally, differences of both OASPL and PWL between the baseline and the other configurations are plotted in Fig. 18. For both low-noise and low-count configurations the trends are captured by the numerical prediction, with discrepancies lower than 1 dB, which is equal to the one-side experimental uncertainty.

V. Time/Circumferential Fourier Analysis and Duct Modal Content

This section reports results of an azimuthal Fourier analysis carried out for the intake lip and bypass exhaust sections. For both, time Fourier transforms have been computed with a bandwidth of 143.1465 Hz and by projecting the numerical solution on a uniform

[¶]An estimation of the dissipation error close to the expected grid cut-off frequency is attempted in the Appendix by computing the sound transmission across a constant-area duct

[**]The tip/vortex interaction frequency would tend to zero if the tip vortices would rotate at the same speed as the fan.

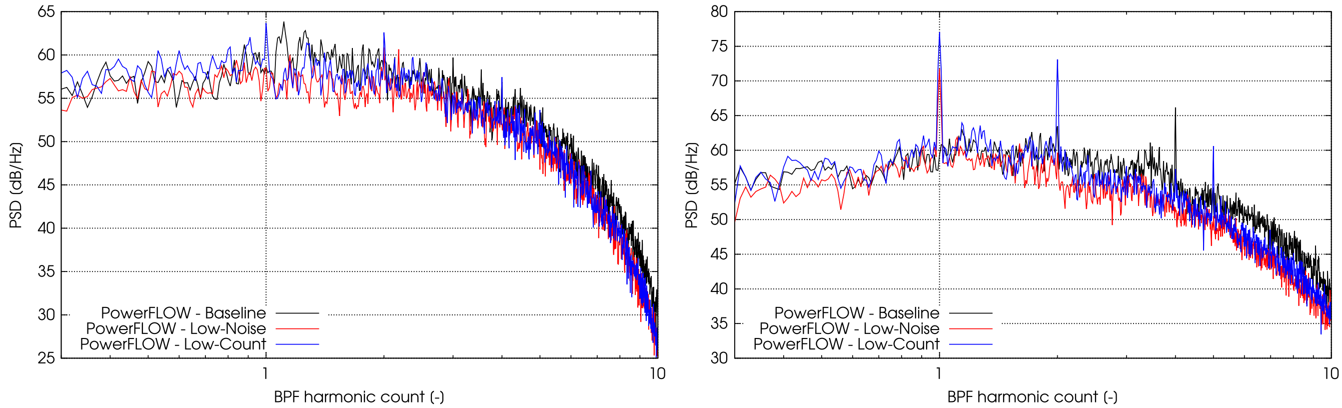

Fig. 16 Effect of OGV configuration on the far-field noise spectra at a distance of 10 m and angular location of 50 deg (left) and 125 deg (right).

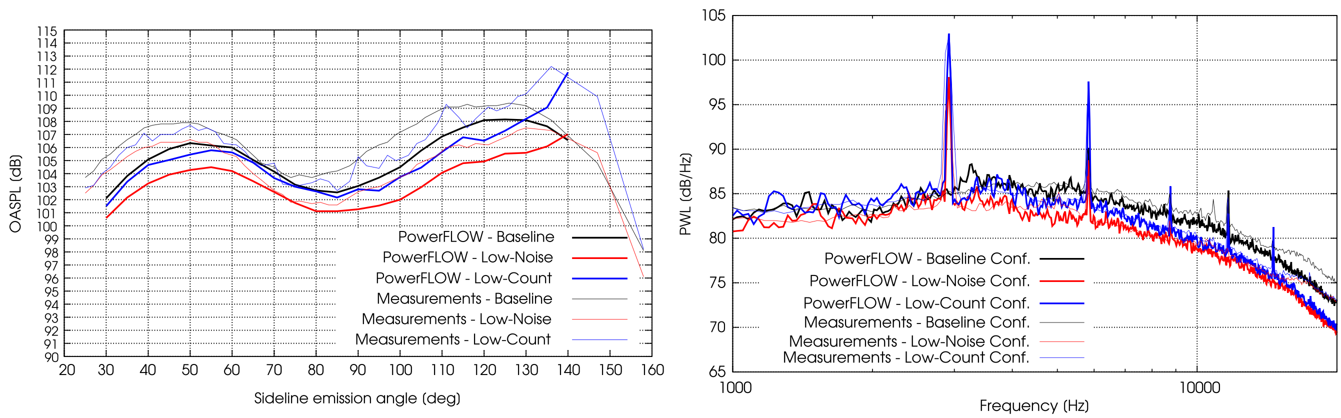

Fig. 17 Absolute far-field OASPL along the sideline array (left) and PWL (right).

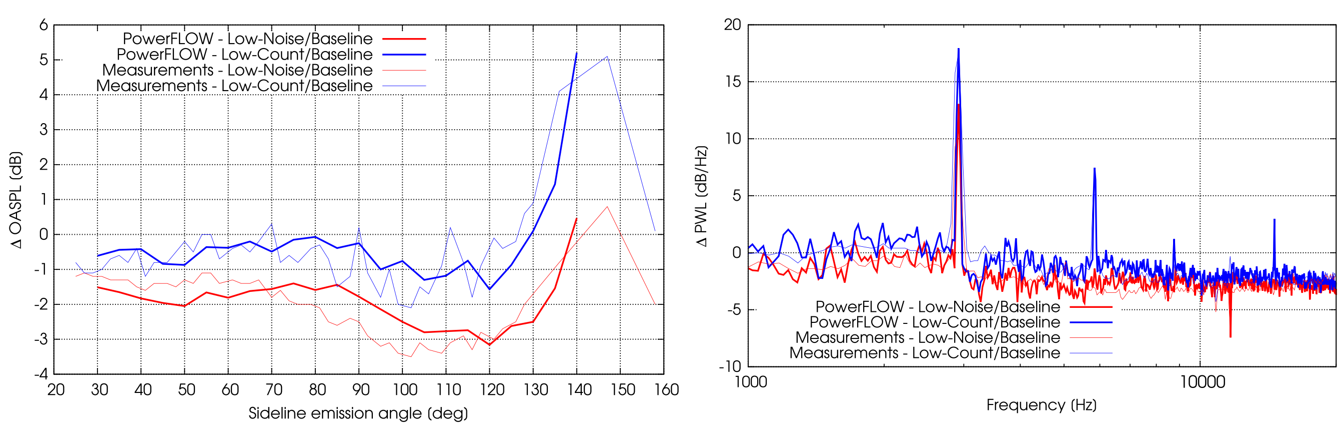

Fig. 18 Relative far-field OASPL along the sideline array (left) and PWL (right).

polar grid of 44 elements in the azimuth and 20 elements in the radial direction. Azimuthal modes in the range $[-24: 24]$ are shown. Duct modes are also extracted on these two sections, through a least-square approach using a modal basis of 65 circumferential modes and five radial modes, with only cut-on modes retained in the basis. The modes are computed for the corresponding annular or hollow circular section and using the integral average Mach number as axial Mach number to compute the duct modes. Upstream and downstream propagating modes are used for the intake lip and bypass exhaust sections, respectively. It should be mentioned, however, that the choice of these two sections, in particular the lip intake one, is not ideal for a projection on a basis of unidirectional infinite straight duct modes.

The reported amplitude values of the Fourier modes are the maximum amplitude of the double Fourier terms along the radius and expressed as SPL. For the duct modes, the PWL is reported, which is computed from the amplitude of the duct mode using the analytical expression of the intensity flux across a section of the duct derived by Rienstra [41] [Eq. (5.2)]. This is consistent with the employed duct modal basis used in the projection process.

Circumferential Fourier modes and duct mode graphs corresponding to narrow-band components around the first and the second BPF are shown, for the baseline configuration, in Fig. 19. The rotor-locked component ($m = 22$) is clearly cut-off in the intake duct. The plane mode, which cannot be justified by any Tyler–Sofrin (T-S) combination, is nonzero both in the intake and bypass ducts, and this can be due to a trapping mechanism involving the engine terminations, and/or the fan/OGV disks as well as, perhaps, a secondary jet column mode. Besides the rotor-locked component, all the circumferential modes at the first BPF cannot be justified by a T-S combination and are therefore due to a modal scattering mechanism involving multiple reflections on the rotor and the stator. An incident

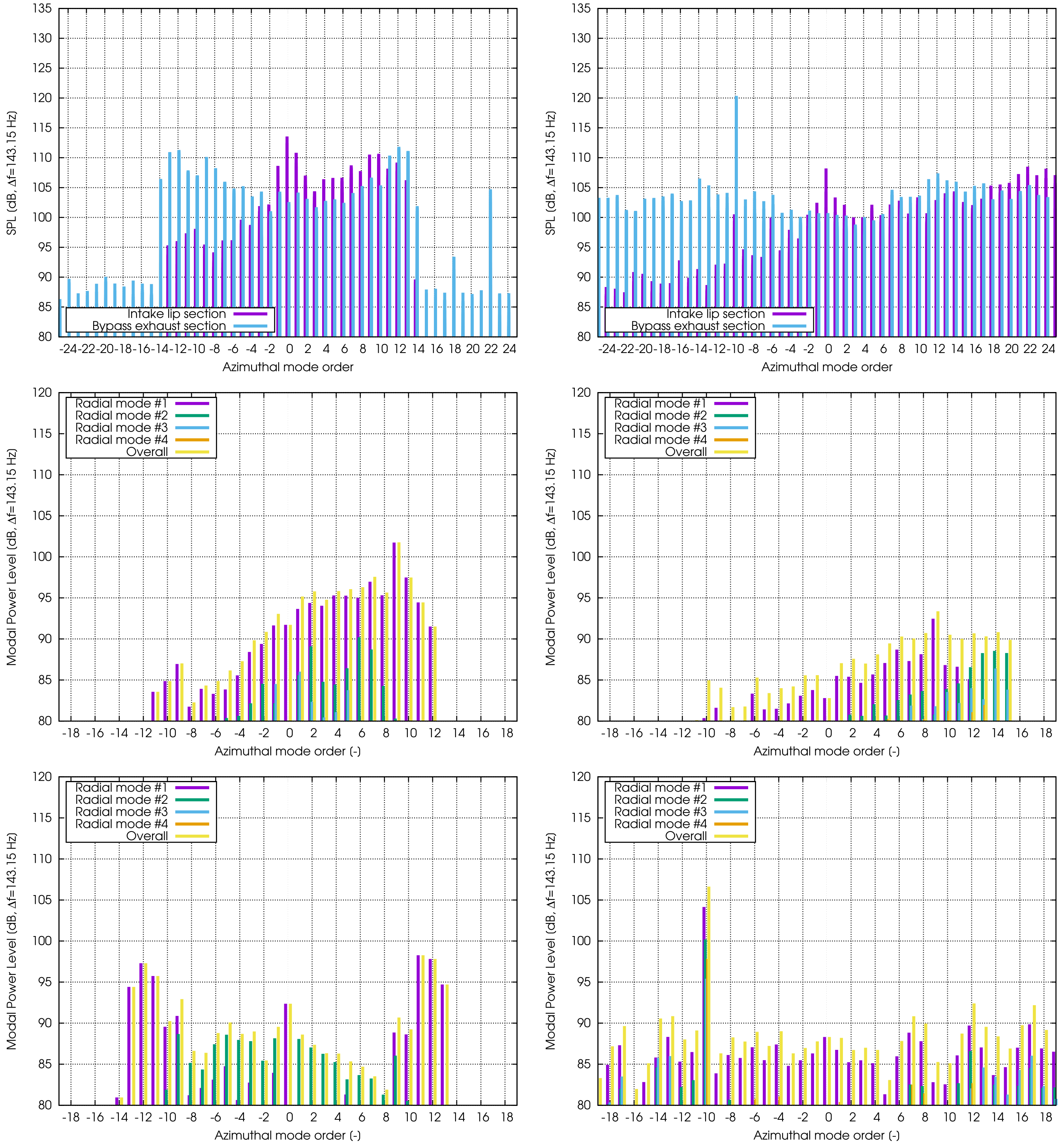

Fig. 19 Circumferential Fourier mode decomposition (top) and cut-on duct modes fitting at the intake lip section (middle) and bypass exhaust section (bottom) for baseline configuration. 1BPF (left) and 2BPF (right) results.

T-S circumferential mode order with the harmonic frequency nBPF ($n > 2$) can be scattered into other T-S circumferential mode orders at 1BPF and 2BPF frequencies. Most other extraneous modes are probably a result of the short time history of the simulation results (10 revolutions) used in the analysis. The random mode contributions are likely not eliminated due to insufficient ensembles when averaging.

The duct mode fitting reveals a rich radial mode content in the intake section, which can be indeed an artifact due to the location of the extraction plane. Conversely, the bypass exhaust section seems to be dominated by the first two radial modes. Interestingly, the power distribution across the modes in the intake duct exhibits a somehow increasing trend from negative to positive circumferential modes. The same trend is clearly visible for the second BPF. Moreover, the bypass section reveals the presence of a strong $m = -10$ mode, which results from a T-S combination ($2 \times 22–1 \times 54$). The first four radial modes contribute to this circumferential mode.

Modes for the low-noise and low-count configurations are shown in Figs. 20 and 21 and exhibit very similar patterns. At 1BPF, the T-S modes -4, -30, and 22 take place in the bypass duct. The mode $m = -4$ is more than 20 dB higher than the others and can be clearly observed also in the intake duct. This is certainly the mode responsible for the far-field 1BPF tone observed in Fig. 16. Because of its low order, this is a mode that tends to have a shallow radiation lobe and is therefore very likely the one responsible for the OASPL increase at high radiation angles observed in Fig. 17. The amplitude

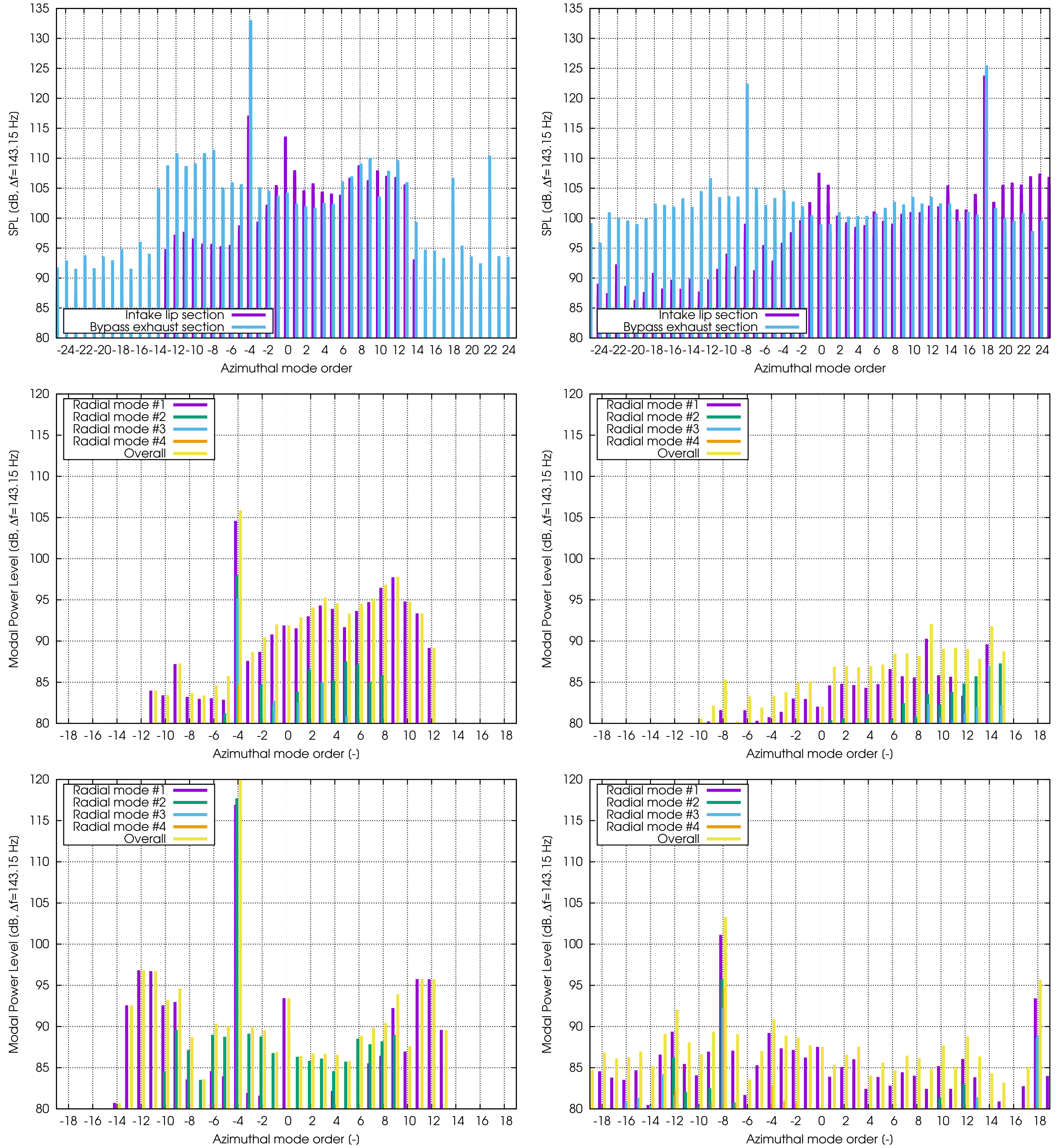

Fig. 20 Circumferential Fourier mode decomposition (top) and cut-on duct modes fitting at the intake lip section (middle) and bypass exhaust section (bottom) for low-count configuration. 1BPF (left) and 2BPF (right) results.

of this mode is about 4 dB higher for the low-count OGV than for the low-noise one, and this can partially explain why the low-count OGV is about 4 dB louder than the low-noise one at 140 deg. At 2BPF, the acoustic field is clearly dominated by two T-S modes: $m = 18$ in both the intake and bypass ducts, and $m = -8$ only in the bypass duct.

A more quantitative analysis can be carried for the baseline configuration by comparing, in Fig. 22, the amplitude of the duct modes $m = -10$ on the bypass exhaust section at 2BPF to values reported by Maunus et al. [42] (Table A2), obtained by the authors at Boston University (BU) solving linearized Euler equations (LEE) in the frequency domain, by Sharma et al. [43] at General Electric using a similar methodology, and through rotating rake measurements, as from Envia et al. [39]. The first radial mode order of the basis is denoted as 1, and the order 0 denotes the overall PWL. The results by BU have been obtained by performing stator-alone simulations and using inflow gust components computed from the hot-wire measurements (BU-LEE/hot-wire) or from rotor wake data extracted from four different steady RANS solutions (BU-LEE/CFD). The LB results show a better agreement with BU-LEE/hot-wire results. In terms of overall PWL (plotted as mode 0), the agreement is within 1 dB. The largest mismatch of about 2.5 dB occurs for the third radial mode.

All the Fourier mode results reveal the importance of modal scattering mechanisms that contribute to enrich the duct modal content. This is clearly a broadband mechanism that can be better visualized looking at a wider frequency range. Following the analysis

Fig. 21 Circumferential Fourier mode decomposition (top) and cut-on duct modes fitting at the intake lip section (middle) and bypass exhaust section (bottom) for low-noise configuration. 1BPF (left) and 2BPF (right) results.

of [20], time/azimuthal Fourier computations with a bandwidth of 715.7325 Hz, a quarter of BPF, in the azimuthal modal range $[-50{:}\,50]$ have been carried out. A polar uniform mesh of 200 circumferential and 20 radial elements has been used. The results are represented as modal amplitude maps, for both the intake and the bypass sections, in Fig. 23. The boundary between cut-on and cut-off modes is visible, with a slight unsymmetrical pattern between negative and positive modes, which is due to the swirling flow effects. The positive modes exhibit slightly larger magnitude than their negative counterparts. Overall, the acoustic field is continuously broad in space and time, and this constitutes a limit to the usage of frequency-domain approaches in the framework of nacelle and liner designs, whereas the present time-domain LB/VLES technology is able to provide a full insight into the broadband modal content of an engine with a turnaround time that is in line with the industrial design cycles.

VI. Effects of the Honeycomb Liner

A. Liner Definition

The SDT fan/OGV configuration was specifically designed with the intent of reducing the tonal noise levels and highlight the broadband noise content. The baseline configuration, in particular, does not reveal any emerging cut-on T-S mode at 1BPF and only one mode in the bypass duct at 2BPF. The noise spectra at 125 deg show peaks at 2BPF and 4BPF. Although these are mostly connected with the noise transmission through and radiation from the bypass duct, a proof-of-concept direct liner simulation was carried out by adding a 1-DOF honeycomb liner in the intake duct only and by tuning this liner to these two harmonics.

The geometrical parameters of a 1-DOF liner are the thickness of the microperforated sheet, the diameter of the orifices, the depth of the underlying honeycombs, and the cross-sectional size of the honeycomb. In the current work, the approximation is made considering one orifice only per honeycomb cell, located in the center. Therefore, the face sheet porosity, which represents the fraction of sheet volume occupied by the fluid, is explicitly related to the cross-sectional side of the honeycomb cell.

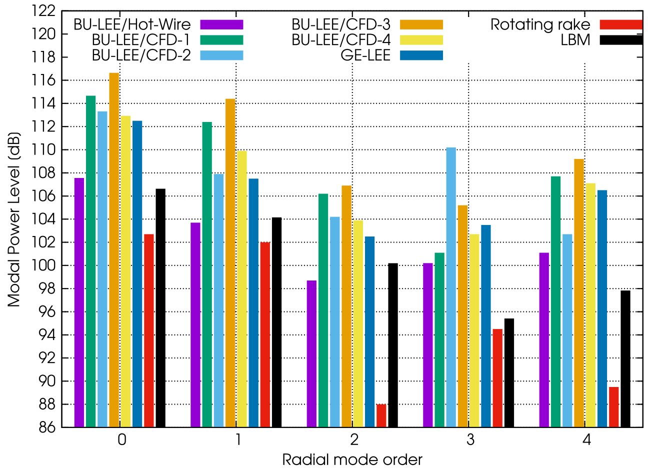

Fig. 22 Duct modes PWL at 2BPF in the bypass exhaust section of the baseline configuration. Azimuthal mode $m = -10$ and radial mode from 1 to 4.

Table 3 1-DOF honeycomb liner design parameters

Honeycomb parameter	Range	Optimal design
Face sheet thickness, mm	[0.5: 2]	0.6
Orifice diameter, mm	[0.8: 1.6]	1.6
Cell diameter, mm	[2.4: 6.8]	6.7
Depth, mm	[0: 50]	32.6
Porosity, %	[10: 50]	5.1

An analytical model of the impedance of 1-DOF liners was derived from Crandall's work [44] by Melling [45]. It models the linear response of the perforated sheet with a mathematical formulation based on a Poiseuille flow inside a pipe excited by acoustic waves. This analytical model was used in the present study to drive an optimum search based on a genetic algorithm with the maximization of the absorption at 1BPF and 2BPF as a target. A single objective was used by attributing a higher weight to the absorption at 2BPF.

Table 3 shows the range of variation of the liner parameters as proposed by Motsinger and Kraft [46], as well as the optimal values.

Mann et al. [34] have evaluated the feasibility of a direct LB/VLES simulation of honeycomb liners. Kundt's tube results for a 1-DOF, a 2-DOF, and a bulk absorber were compared to analytical and semi-empirical results. Grid-converged solutions in good agreement with the theoretical solutions were achieved. The same approach has been used in the present study to verify the behavior of the optimal liner defined through the theoretical model. A Kundt's tube simulation has been therefore carried out by using the finest mesh resolution available in the tripped simulation setup (0.0915 mm).

The optimal liner is depicted in Fig. 24, together with a comparison between the simulated and the theoretical absorption curves. The first peak at about 0.5 BPF represents the Helmholtz-type resonance of the honeycomb, which can be approximated by $f_{\mathrm{HR}} = \sqrt{S/(l'V)}c_\infty/(2\pi)$, where S is the area of a perforation, l' is

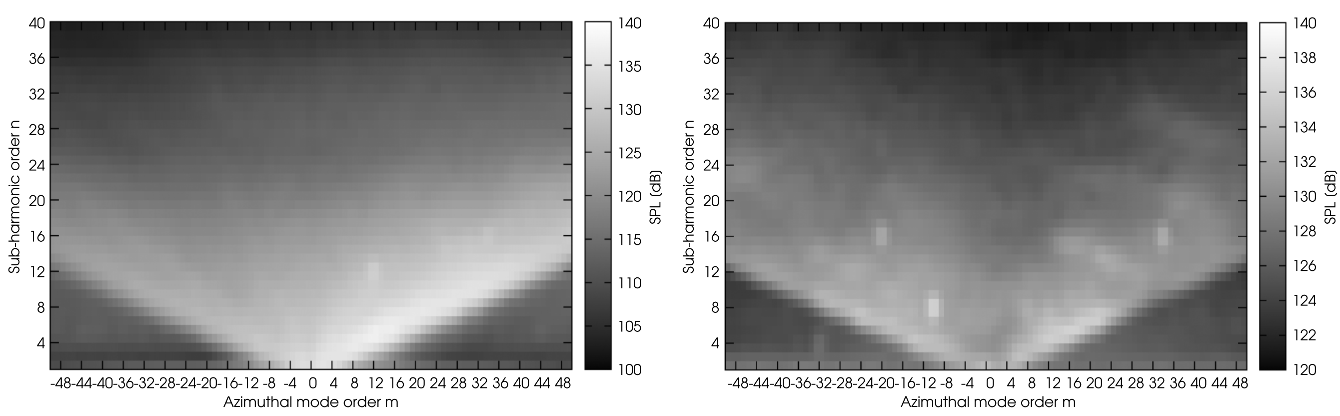

Fig. 23 Time/circumferential Fourier component maps: intake lip section (left) and bypass exhaust section (right).

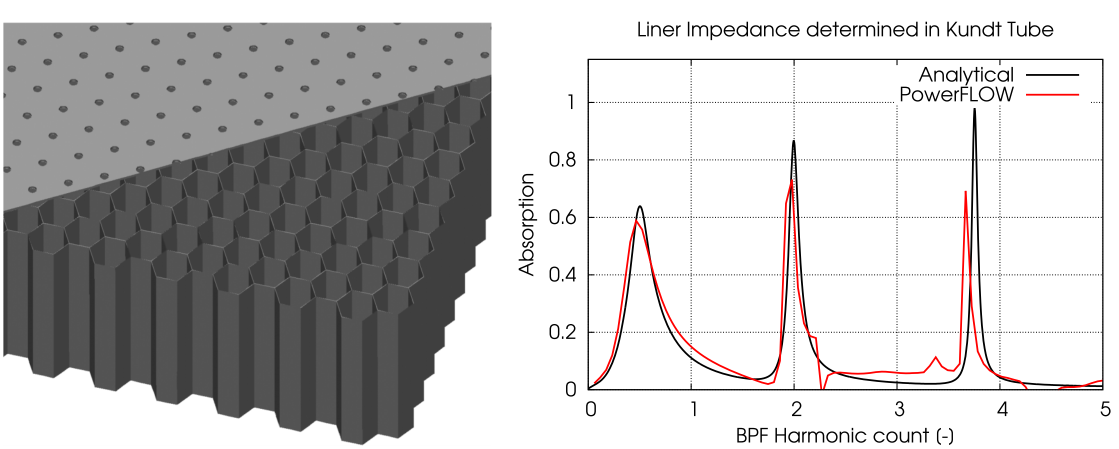

Fig. 24 1-DOF liner with the aim of high absorption at 2BPF: liner geometry (left) and its absorption (right).

the face sheet thickness incorporating an opening correction, and V is the volume of a honeycomb cell. The second resonance corresponds to a $\lambda/2$ standing wave along the honeycomb depth, whereas the third peak is a harmonic of this standing wave. This is an approximated interpretation of the resonance modes because the Helmholtz resonance and the standing-wave resonances are coupled, which results in a frequency shift of the peaks. This explains why the second harmonic of the standing wave at 2BPF is not exactly at 4BPF. Locating the Helmholtz resonance at a frequency lower then 1BPF could be useful to attenuate the subharmonic components due to the interaction between the rotor tip vortices and the blades. Despite the discrepancies at higher frequencies, which are mainly caused by the constraints on the diameter of the Kundt's tube to avoid the occurrence of nonplanar cut-on modes up to 5BPF, the current setup is considered adequate to a conceptual study.

By using a morphing procedure, the liner of Fig. 24 was transformed into an annular zero-splice liner and installed in the intake of the SDT baseline configuration, as illustrated in Fig. 1. The computational setup is derived from the baseline setup, by using the finest mesh resolution to fill the liner orifices. The number of FEV and the CPU time are 69 and 40% higher than for the baseline simulation, respectively.

B. Near-Field Effects and Flow Features

Figure 25 shows the locations of three probes close to the intake liner, located at a distance of about 10 mm from the wall. For each probe, pressure spectra are computed for the baseline and the treated cases and compared by plotting the difference of the corresponding narrow-band spectra. These results are in agreement with the absorption curve of Fig. 24. However, because of the properties of noise transmission through a duct, a reduction of the in-duct near-field pressure levels does not correspond to a comparable far-field noise reduction.

Figure 26 shows an instantaneous view of wall-normal velocity field in the honeycomb cells. A quite well-established periodic pattern can be observed. The honeycomb cells behave like Helmholtz resonators under grazing flow conditions. To visualize the liner behavior at the resonance frequencies, narrow-band sound pressure levels (SPL) of the unsteady flowfield in a plane through the honeycomb are computed and visualized in Fig. 27 for the Helmholtz resonance frequency and 2BPF. As expected, a standing-wave pattern can be observed only for 2BPF (first cavity resonance mode). The standing wave exhibits one node at a certain distance from the backplate as a consequence of the destructive interference between two waves of wavelength twice the honeycomb depth.

C. Far-Field Effects

The effects of the intake liner on the far-field noise levels are illustrated in this subsection. Noise spectra at a forward microphone location of 50 deg and a distance of 10 m are plotted in Fig. 28 for the baseline and treated configurations. These spectra have been computed by integration on the whole FW-H surface of Fig. 3, the intake hemisphere only, and the exhaust cone only. As expected, the liner mitigates the far-field noise, but this is only due to a reduction of the intake contribution.

Finally, Fig. 29 shows the OASPL and the PWL spectrum for the baseline and treated simulations. A noise attenuation of about 2.5 dB in the forward radiation arc can be observed. Unfortunately, because of the absence of liner in the bypass duct, the tonal peaks in the PWL spectrum are almost unaffected by the presence of the liner because these are radiated from the exhaust. The liner is therefore acting in a broad frequency range, and it is not straightforward to establish the

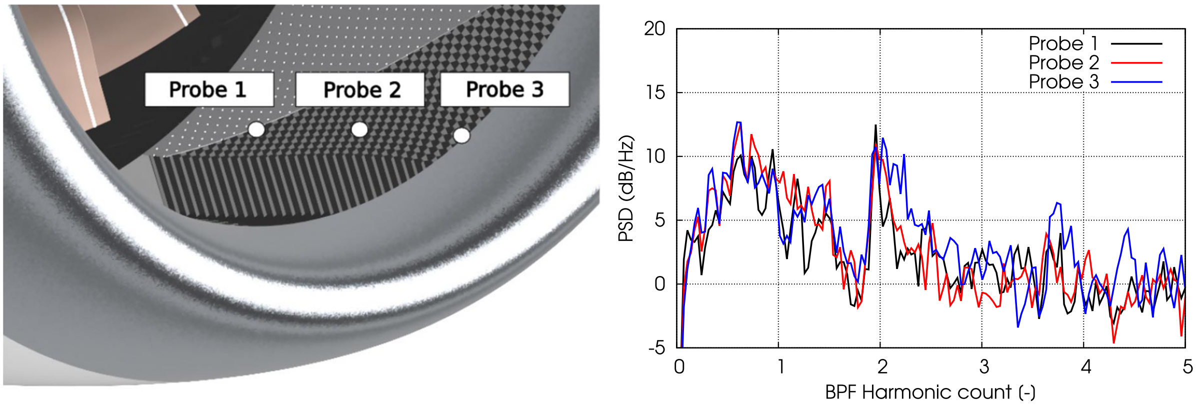

Fig. 25 Near-field probes (left) and corresponding near-field narrow-band spectra (right) plotted as difference between baseline and treated configuration results.

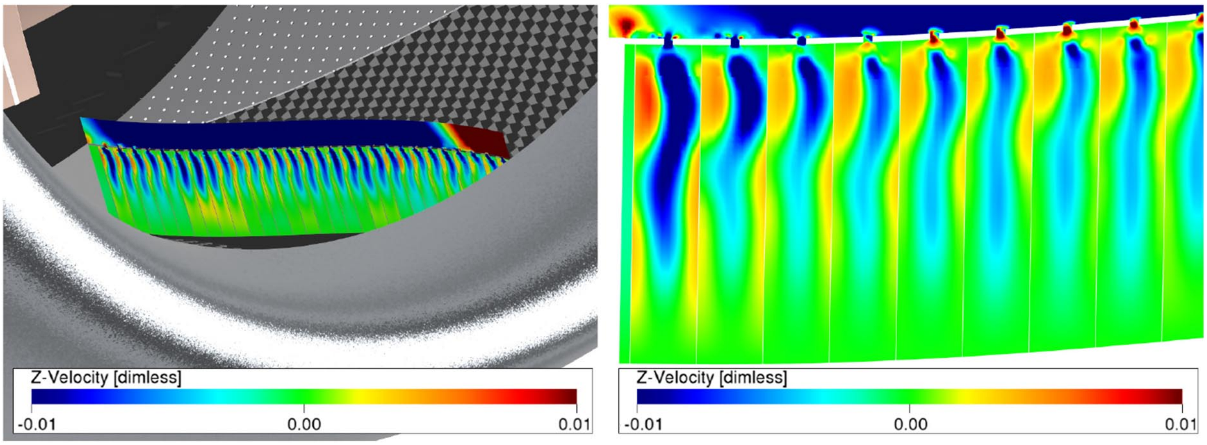

Fig. 26 Wall-normal velocity normalized by the maximum velocity at the rotor tip in a plane cutting through the honeycomb.

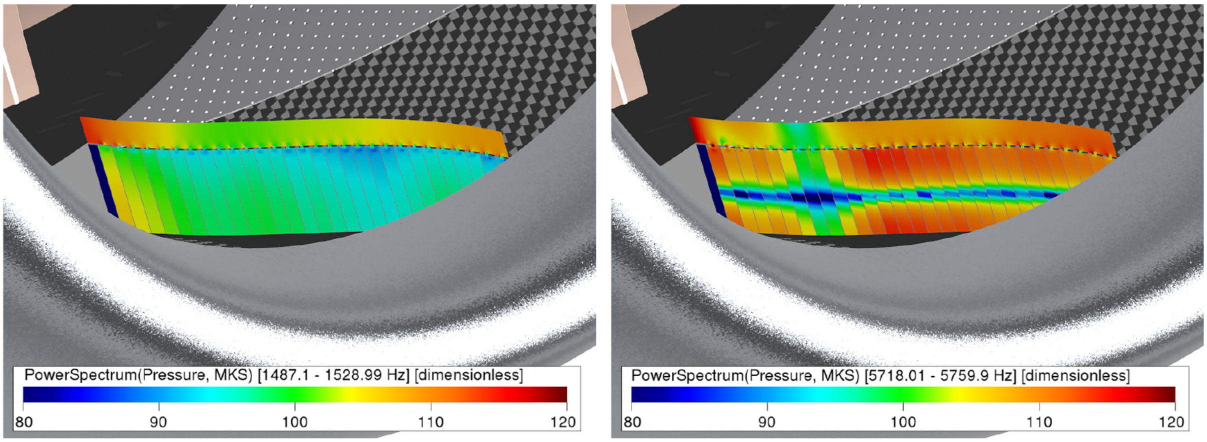

Fig. 27 SPL field in plane cutting through the honeycomb computed in narrow bands around resonance frequencies: Helmholtz resonance (left), and 2BPF (right).

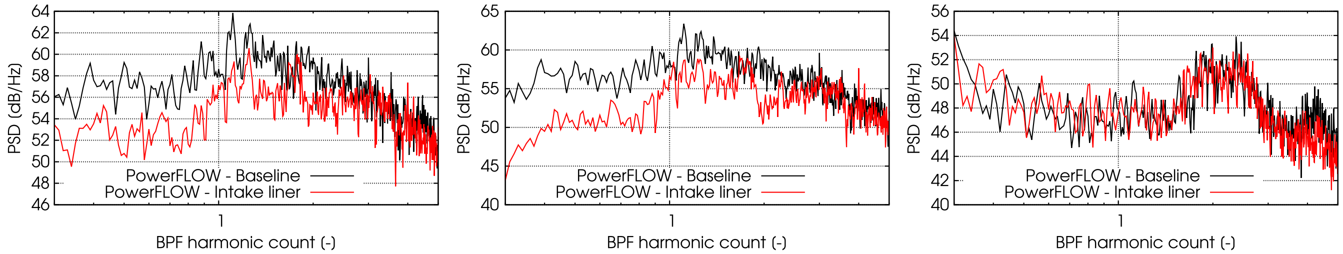

Fig. 28 Effect of the intake liner on the far-field noise spectra. Overall FW-H integration surface on the left, intake contribution in the middle, and exhaust contribution on the right.

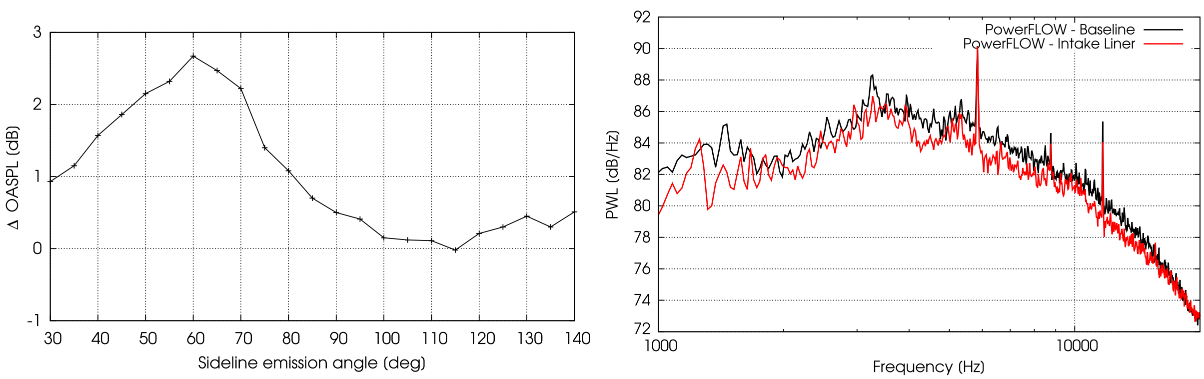

Fig 29 Effect of the intake liner on the far-field OASPL along the sideline array (left) and on the PWL spectrum (right).

amount of acoustic energy absorbed through Helmholtz resonance or standing-wave mechanisms.

VII. Conclusions

The 22-in SDT fan/outlet guide vane (OGV) experiment of NASA Glenn Research Center was reproduced numerically using an lattice-Boltzmann/very large-eddy simulation flow solver. Three OGV configurations and one rotational speed were considered, corresponding to an approach flight condition. Because of a combination of factors related to the possible transitional nature of the boundary layer on the rotor blades and to the employed mesh resolution, using a trip on the suction side of the rotor blade improved the prediction of the velocity broadband spectra in the rotor wake at relative radial locations lower than about 60%. Comparisons with available measurements of the noise power level and far-field overall sound pressure level (OASPL) revealed consistent trends between the three OGV configurations. In particular, the predicted OASPL differences between the baseline and the low-noise OGVs were found in less than 1 dB agreement with the measurements. Some of the findings for the low-noise and low-count configurations need to be confirmed by further analyses of the experimental data. A time/circumferential Fourier analysis of the computed field revealed the broadband nature in time and space of the acoustic field, thus motivating the usage of time-domain solutions for nacelle and liner design and optimizations. The computational turnaround time was in the order of one week per design on a 720-core cluster, which is compatible with the development time of a new engine. Finally, the feasibility of simulations including a honeycomb liner was investigated as an alternative to the usage of a wall impedance model. Future efforts will be focused on the simulation of additional operating conditions and on the extension of the validation basis to other measured quantities.

Appendix: Estimation of the Grid Cut-Off Frequency

In this Appendix, sound transmission though a constant-area duct is computed with the goal of evaluating the acoustic propagation error in the intake of the full engine simulation. This is not an easy task because of the broadband nature of the original problem and the multimodal character of the high-frequency spectrum.

An annular duct of radial ratio $r_1/r_2 = 0.3$ is considered, which corresponds to the fan plane section of the SDT engine. Two spinning modes of azimuthal mode order $m = 20$ and $m = 40$ and second radial mode are considered. The Helmholtz number is $kr_2 = 51.85$, corresponding to a frequency of 10 kHz. The mode $m = 20$ has a cut-on/cut-off ratio equal to 0.534, whereas the mode $m = 40$ is almost cut-off, with a cut-on/cut-off ratio equal to 0.952. The choice of these two modes is arbitrary, but considering two different cut-on/cut-off ratios gives a more general indication of the solver accuracy in transmitting the noise from the fan plane to the intake lip and beyond. The duct has an axial extension $L_x = 4r_2$. The acoustic mode is prescribed as a Dirichlet boundary condition for pressure and the three components of the velocity on the right termination of the duct. A numerical sponge is set from the left termination to $3r_2$ on the right. Slip wall conditions are imposed on the inner and outer walls of the duct. Computations are performed by using a constant mesh generated by setting four values of the lattice resolution corresponding to 8.7 (coarse), 11.5 (medium), 17.3 (fine), and 23.1 (extra fine) number of points per acoustic wavelength (N_{ppw}). The medium resolution ($N_{ppw} = 11.5$) corresponds to the resolution used in the SDT computation inside the FW-H integration surface, whereas the extrafine resolution ($N_{ppw} = 23.1$) is used in the intake duct, from the sliding mesh boundary to the intake lip. The sponge damping parameter is increased exponentially from 0 to a maximum value at the duct termination. The same maximum value is used for all cases, thus resulting in an artificial dissipation coefficient inversely proportional to the square of the lattice resolution.

Contour plots of the SPL integrated around the tonal frequency are shown in Fig. A1. For the sake of comparison, the solutions have been projected on a constant-size Cartesian grid consisting of 39 points in the duct cross section. The damping in the sponge region is less pronounced for higher resolutions. Values are referred to the maximum SPL of the analytical solution. Both modes are expected to be transmitted without attenuation along the duct. Deviations from this behavior can be observed for lower mesh resolutions, and in particular for the second case, which exhibits modulations in the sponge region, which could be the consequence of a numerical cut-on/cut-off transition with consequent back reflection. It should be pointed out that the higher errors for the second mode can be related to the higher cut-on/cut-off ratio, as well as to the lower azimuthal resolution of the mode.

The SPL extracted along an axial line cut at a distance r_2 from the inlet boundary condition (green line) is plotted as a function of the radial location in Fig. A2, together with the analytical solution. Values are referred to the maximum SPL of the analytical solution. For the first mode, an error of about 1 dB is cumulated over a distance equal to the outer duct radius when the medium resolution is used, whereas the error for the extrafine resolution is significantly smaller. Hence, because the maximum distance between the FW-H surface and the intake lip is of the order of r_2, it should be argued that, at 10 kHz, the propagation error is in the order of 1 dB. Unfortunately, the ΔdB errors are about two times higher for the second mode.

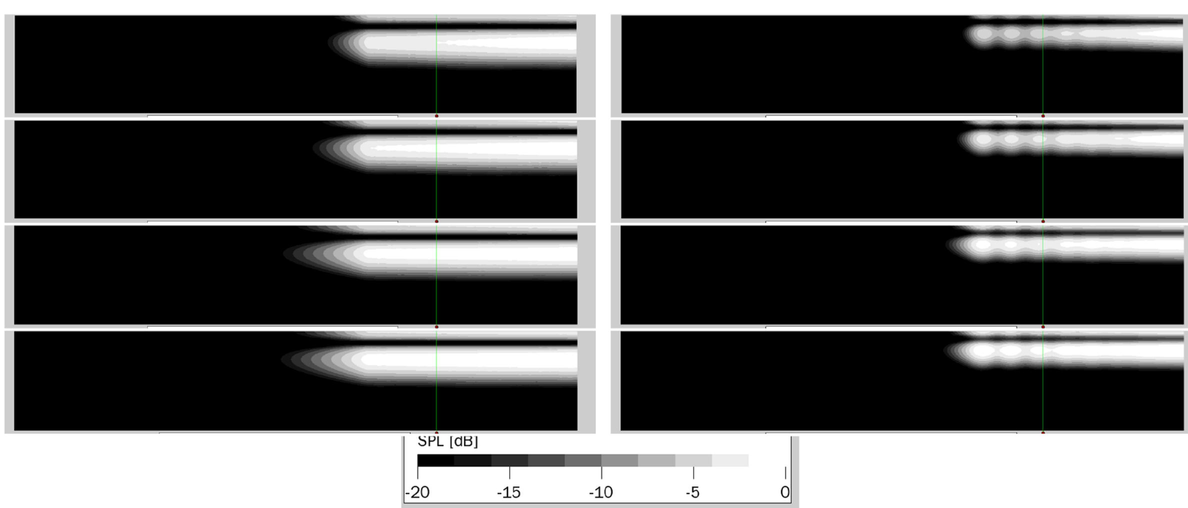

Fig. A1 SPL of modes $m = 20$ (left) and $m = 40$ (right) computed with different mesh resolutions, from coarse (top) to extra fine (bottom).

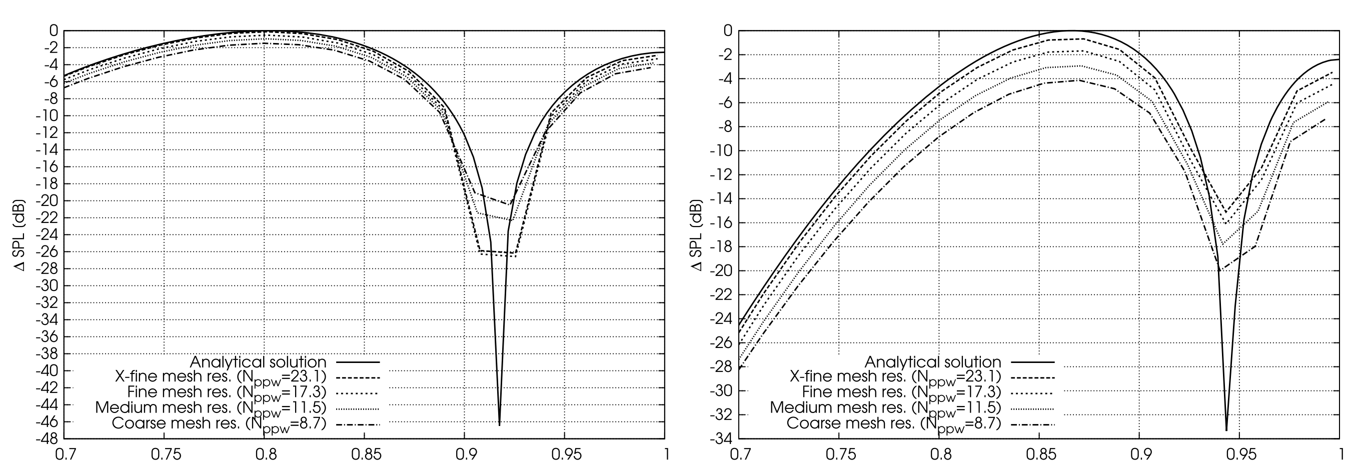

Fig. A2 Duct cross-sectional SPL at a distance r_2 from the inlet. Comparison between analytical solution and numerical solutions for different lattices resolutions. Mode $m = 20$ on the left, and $m = 40$ on the right.

Therefore, it is not immediate to evaluate the exact error for the SDT computations. Finally, at a frequency of 20 kHz, errors of the order of those obtained using the coarse resolution, say in the range of 2–4 dB, should be expected.

Acknowledgment

The authors wish to acknowledge Edmane Envia from NASA Glenn Research Center for providing the geometry and experimental data of the NASA 22-in fan source diagnostic test.

References

[1] Chen, H., Chen, S., and Matthaeus, W., "Recovery of the Navier–Stokes Equations Using a Lattice-Gas Boltzmann Method," *Physical Review A*, Vol. 45, No. 8, 1992, pp. R5339–R5342. doi:10.1103/PhysRevA.45.R5339

[2] Chen, H., Kandasamy, S., Orszag, S. A., Succi, S., and Yakhot, V., "Extended Boltzmann Kinetic Equation for Turbulent Flows," *Science*, Vol. 301, No. 5633, 2003, pp. 633–636. doi:10.1126/science.1085048

[3] Chen, H., Orszag, S., Staroselsky, I., and Succi, S., "Expanded Analogy Between Boltzmann Kinetic Theory of Fluid and Turbulence," *Journal of Fluid Mechanics*, Vol. 519, Nov. 2004, pp. 301–314. doi:10.1017/S0022112004001211

[4] Shan, X., Yuan, X.-F., and Chen, H., "Kinetic Theory Representation of Hydrodynamics: A Way Beyond the Navier–Stokes Equation," *Journal of Fluid Mechanics*, Vol. 550, March 2006, pp. 413–441. doi:10.1017/S0022112005008153

[5] Brès, G. A., Pérot, F., and Freed, D. M., "Properties of the Lattice-Boltzmann Method for Acoustics," *15th AIAA/CEAS Aeroacoustics Conference*, AIAA Paper 2009-3395, May 2009.

[6] Marié, S., Ricot, D., and Sagaut, P., "Comparison Between Lattice Boltzmann Method and Navier Stokes High Order Schemes for Computational Aeroacoustics," *Journal of Computational Physics*, Vol. 228, No. 4, 2009, pp. 1056–1070. doi:10.1016/j.jcp.2008.10.021

[7] Casalino, D., Ribeiro, A. F. P., Fares, E., and Nölting, S., "Lattice-Boltzmann Aeroacoustic Analysis of the LAGOON Landing Gear Configuration," *AIAA Journal*, Vol. 52, No. 6, 2014, pp. 1232–1248. doi:10.2514/1.J052365

[8] Casalino, D., Ribeiro, A. F. P., and Fares, E., "Facing Rim Cavities Fluctuation Modes," *Journal of Sound and Vibration*, Vol. 333, No. 13, 2014, pp. 2812–2830. doi:10.1016/j.jsv.2014.01.028

[9] Khorrami, M. R., Fares, E., and Casalino, D., "Towards Full Aircraft Airframe Noise Prediction: Lattice Boltzmann Simulations," *20th AIAA/CEAS Aeroacoustics Conference*, AIAA Paper 2014-2481, June 2014.

[10] Fares, E., Casalino, D., and Khorrami, M., "Evaluation of Airframe Noise Reduction Concepts via Simulations Using a Lattice Boltzmann Approach," AIAA Paper 2015-2988, 2015.

[11] Brès, G. A., Freed, D. M., Wessels, M., Noelting, S., and Pérot, F., "Flow and Noise Predictions for the Tandem Cylinder Aeroacoustic Benchmark," *Physics of Fluids*, Vol. 24, No. 3, March 2012, Paper 036101.

[12] Hao, J., Kotapati, R. B., Pérot, F., and Mann, A., "Numerical Studies of Acoustic Diffraction by Rigid Bodies," *22nd AIAA/CEAS Aeroacoustics Conference*, AIAA Paper 2016-2705, 2016.

[13] Glegg, S. A. L., "The Response of a Swept Blade Row to a Three-Dimensional Gust," *Journal of Sound and Vibration*, Vol. 227, No. 1, Oct. 1999, pp. 29–64. doi:10.1006/jsvi.1999.2327

[14] Posson, H., Moreau, S., and Roger, M., "On the Use of a Uniformly Valid Analytical Cascade Response Function for Fan Broadband Noise Predictions," *Journal of Sound and Vibration*, Vol. 329, No. 18, 2010, pp. 3721–3743. doi:10.1016/j.jsv.2010.03.009

[15] Grace, S., "Fan Broadband Interaction Noise Modeling Using a Low-Order Method," *Journal of Sound and Vibration*, Vol. 346, June 2015, pp. 402–423. doi:10.1016/j.jsv.2015.02.013

[16] Ventres, C. S., Theobald, M. A., and Mark, W. D., "Turbofan Noise Generation, Volume 1: Analysis," NASA CR-167952, 1982.

[17] Hanson, D. B., "Theory for Broadband Noise of Rotor and Stator Cascades with Inhomogeneous Inflow Turbulence Including Effects of Lean and Sweep," NASA CR-2001-210762, May 2001.

[18] Posson, H., Moreau, S., and Roger, M., "On a Uniformly Valid Analytical Rectilinear Cascade Response Function," *Journal of Fluid Mechanics*, Vol. 663, Nov. 2010, pp. 22–52. doi:10.1017/S0022112010003368

[19] Posson, H., Moreau, S., and Roger, M., "Broadband Noise Prediction of Fan Outlet Guide Vane Using a Cascade Response Function," *Journal of Sound and Vibration*, Vol. 330, No. 25, 2011, pp. 6153–6183. doi:10.1016/j.jsv.2011.07.040

[20] Posson, H., and Moreau, S., "Effect of Rotor Shielding on Fan-Outlet Guide Vanes Broadband Noise Prediction," *AIAA Journal*, Vol. 51, No. 7, 2013, pp. 1576–1592. doi:10.2514/1.J051784

[21] Cooper, A. J., and Peake, N., "Trapped Acoustic Modes in Aeroengine Intakes with Swirling Flows," *Journal of Fluid Mechanics*, Vol. 419, Sept. 2000, pp. 151–175. doi:10.1017/S0022112000001245

[22] Hanson, D. B., "Mode Trapping in Coupled 2D Cascades—Aerodynamic and Acoustic Results," *15th Aeroacoustics Conference*, AIAA Paper 1993-4417, 1993.

[23] Premo, J., and Joppa, P., "Fan Noise Source Diagnostic Test–Wall Measured Circumferential Array Mode Results," *8th AIAA/CEAS Aeroacoustics Conference & Exhibit*, AIAA Paper 2002-2429, June 2002.

[24] Nallasamy, M., and Envia, E., "Computation of Rotor Wake Turbulence Noise," *Journal of Sound and Vibration*, Vol. 282, Nos. 3–5, 2005, pp. 649–678. doi:10.1016/j.jsv.2004.03.062

[25] Grace, S., "Influence of Model Parameters and the Vane Response Method on a Low-Order Prediction of Fan Broadband Noise," *International Journal of Aeroacoustics*, Vol. 15, Nos. 1–2, 2016, pp. 131–143. doi:10.1177/1475472X15627407

[26] Mann, A., Pérot, F., Kim, M.-S., Casalino, D., and Fares, E., "Advanced Noise Control Fan Direct Aeroacoustics Predictions Using a Lattice-Boltzmann Method," *18th AIAA/CEAS Aeroacoustics Conference*, AIAA Paper 2012-2287, June 2012.

[27] Sutliff, D. L., "Rotating Rake Turbofan Duct Mode Measurement System," NASA TM-2005-213828, 2005.

[28] Pérot, F., Mann, A., Kim, M.-S., and Casalino, E. F. D., "Investigation of Inflow Condition Effects on the ANCF Aeroacoustics Radiation Using LBM, " *INTER-NOISE and NOISE-CON Congress and Conference Proceedings*, Proceedings of InterNoise, New York, 2012, http://www.ingentaconnect.com/content/ince/incecp/2012/00002012/00000007.

[29] Casalino, D., Ribeiro, A. F. P., Fares, E., Nölting, S., Mann, A., Pérot, F., Li, Y., Lew, P.-T., Sun, C., Gopalakrishnan, P., Zhang, R., Chen, H., and Habibi, K., "Towards Lattice-Boltzmann Prediction of Turbofan Engine Noise," *20th AIAA/CEAS Aeroacoustics Conference*, AIAA Paper 2014-3101, 2014.

[30] Sanjose, M., Daroukh, M., Magnet, W., laborderie, J. D., Moreau, S., and Mann, A., "Tonal Fan Noise Prediction and Validation on the ANCF Configuration," *Proceedings of the International Conference on Fan Noise, Technology and Numerical Methods*, Lyon, France, April 2015.

[31] Woodward, R. P., Hughes, C., Jeracki, R., and Miller, C., "Fan Noise Source Diagnostic Test—Far-Field Acoustic Results," *8th AIAA/CEAS Aeroacoustics Conference & Exhibit*, AIAA Paper 2002-2427, June 2002.

[32] Envia, E., "Fan Noise Source Diagnostic Test – Vane Unsteady Pressure Results," *8th AIAA/CEAS Aeroacoustics Conference & Exhibit*, AIAA Paper 2002-2430, June 2002.

[33] Pérot, F., Freed, D. M., and Mann, A., "Acoustic Absorption of Porous Materials Using LBM," *19th AIAA/CEAS Aeroacoustics Conference*, AIAA Paper 2013-2070, May 2013.

[34] Mann, A., Pérot, F., Kim, M.-S., and Casalino, D., "Characterization of Acoustic Liners Absorption Using a Lattice-Boltzmann Method," *19th AIAA/CEAS Aeroacoustics Conference*, AIAA Paper 2013-2271, May 2013.

[35] Brès, G. A., Pérot, F., and Freed, D. M., "A Ffowcs Williams–Hawkings Solver for Lattice-Boltzmann Based Computational Aeroacoustics," *16th AIAA/CEAS Aeroacoustics Conference*, AIAA Paper 2010-3711, June 2010.

[36] Najafi-Yazdi, A., Brès, G. A., and Mongeau, L., "An Acoustic Analogy Formulation for Moving Sources in Uniformly Moving Media," *Proceeding of the Royal Society of London A*, Vol. 467, No. 2125, 2011, pp. 144–165. doi:10.1098/rspa.2010.0172

[37] Chen, H., Teixeira, C. M., and Molvig, K., "Digital Physics Approach to Computational Fluid Dynamics: Some Basic Theoretical Features," *International Journal of Modern Physics C*, Vol. 8, No. 4, 1997, pp. 675–684. doi:10.1142/S0129183197000576

[38] Chen, H., Teixeira, C., and Molvig, K., "Realization of Fluid Boundary Conditions via Discrete Boltzmann Dynamics," *International Journal*

of Modern Physics C, Vol. 9, No. 8, 1998, pp. 1281–1292.
doi:10.1142/S0129183198001151

[39] Envia, E., Tweedt, D. L., Woodward, R. P., Elliot, D. M., Fite, E., Hughes, C. H., Podboy, G. C., and Sutliff, D. L., "An Assessment of Current Fan Noise Prediction Capabilities," *14th AIAA/CEAS Aeroacoustics Conference*, AIAA Paper 2008-2991, May 2008.

[40] Casalino, D., Hazir, A., and Mann, A., "Turbofan Broadband Noise Prediction Using the Lattice Boltzmann Method," *22nd AIAA/CEAS Aeroacoustics Conference*, AIAA Paper 2016-2945, 2016.

[41] Rienstra, S. W., "Sound Transmission in Slowly Varying Circular and Annular Lined Ducts with Flow," *Journal of Fluid Mechanics*, Vol. 380, Feb. 1999, pp. 279–296.
doi:10.1017/S0022112098003607

[42] Maunus, J., Grace, S., and Sondak, D., "Effect of Rotor Wake Structure on Fan Interaction Tone Noise," *AIAA Journal*, Vol. 50, No. 4, 2012, pp. 818–831.
doi:10.2514/1.J051068

[43] Sharma, A., Richards, S., Wood, T., and Shieh, C., "Numerical Prediction of Exhaust Fan Tone Noise from High Bypass Aircraft Engines," *AIAA Journal*, Vol. 47, No. 12, 2009, pp. 2866–2879.
doi:10.2514/1.42208

[44] Crandall, I. B., *Theory of Vibrating Systems and Sound*, D. Van Nostrand, New York, 1926.

[45] Melling, T. H., "The Acoustic Impedance of Perforates at Medium and High Sound Pressure Levels," *Journal of Sound and Vibration*, Vol. 29, No. 1, 1973, pp. 1–65.
doi:10.1016/S0022-460X(73)80125-7

[46] Motsinger, R. E., and Kraft, R. E., "Design and Performance of Duct Acoustic Treatment," *Aeroacoustics of Flight Vehicles: Theory and Practice, Volume 2: Noise Control*, edited by H. F. Nelson, NASA, Hampton, VA, 1991, pp. 165–206.

M. M. Choudhari
Associate Editor